Cross-Modality Coherent Registration of Whole Mouse Brains

Hanchuan Peng (h@braintell.org)
Allen Institute for Brain Science

Lei Qu
Key Laboratory of Intelligent Computation & Signal Processing, Ministry of Education, Anhui University
https://orcid.org/0000-0002-2129-5253

Yuanyuan Li
Key Laboratory of Intelligent Computation & Signal Processing, Ministry of Education, Anhui University

Peng Xie
SEU-ALLEN Joint Center, Institute for Brain and Intelligence, Southeast University

Lijuan Liu
Institute for Brain and Intelligence, Southeast University

Yimin Wang
Institute for Brain and Intelligence, Southeast University https://orcid.org/0000-0003-2515-6602

Jun Wu
Key Laboratory of Intelligent Computation & Signal Processing, Ministry of Education, Anhui University

Yu Liu
Key Laboratory of Intelligent Computation & Signal Processing, Ministry of Education, Anhui University

Tao Wang
Key Laboratory of Intelligent Computation & Signal Processing, Ministry of Education, Anhui University

Longfei Li
Key Laboratory of Intelligent Computation & Signal Processing, Ministry of Education, Anhui University

Kaixuan Guo
Key Laboratory of Intelligent Computation & Signal Processing, Ministry of Education, Anhui University

Wan Wan
Key Laboratory of Intelligent Computation & Signal Processing, Ministry of Education, Anhui University

Lei Ouyang
Key Laboratory of Intelligent Computation & Signal Processing, Ministry of Education, Anhui University

Feng Xiong
SEU-ALLEN Joint Center, Institute for Brain and Intelligence, Southeast University

Yefeng Zheng
Tencent Jarvis Lab

Fang Xu
CAS Key Laboratory of Brain Connectome and Manipulation

Hui Gong
Britton Chance Center for Biomedical Photonics,Wuhan National Laboratory for Optoelectronics,MoE Key Laboratory for Biomedical Photonics, Huazhong University of Science and Technology
Hongwei Dong
Center for Integrative Connectomics, Department of Neurobiology, David Geffen School of Medicine at UCLA
Qingming Luo
Hainan University
Guo-Qiang Bi
Hefei National Laboratory for Physical Sciences at the Microscale, and School of Life Sciences, University of Science and Technology of China
Michael Hawrylycz
Allen Institute for Brain Science https://orcid.org/0000-0002-5741-8024
Hongkui Zeng
Allen Institute for Brain Science https://orcid.org/0000-0002-0326-5878

Article

Keywords: brain mapping, 3D-imaging, mBrainAligner, Allen Common Coordinate Framework atlas

Posted Date: March 30th, 2021

DOI: https://doi.org/10.21203/rs.3.rs-321118/v1

Version of Record: A version of this preprint was published at Nature Methods on December 9th, 2021. See the published version at https://doi.org/10.1038/s41592-021-01334-w.

Cross-Modality Coherent Registration of Whole Mouse Brains

Abstract: Recent whole brain mapping projects are collecting large-scale 3D images using powerful and informative modalities, such as STPT, fMOST, VISoR, or MRI. Registration of these multi-dimensional whole-brain images onto a standard atlas is essential for characterizing neuron types and constructing brain wiring diagrams. However, cross-modality image registration is challenging due to intrinsic variations of brain anatomy and artifacts resulted from different sample preparation methods and imaging modalities. We introduced a cross-modality registration method, called mBrainAligner, which uses coherent landmark mapping as well as deep neural networks to align whole mouse brain images to the standard Allen Common Coordinate Framework atlas. We also built a single cell resolution atlas using the fMOST modality, and used our method to generate whole brain map of 3D full single neuron morphology and neuron cell types.

INTRODUCTION

Recent advances in high-resolution light microscopy [1-6], tissue clearing [7-13], sparse labeling techniques [2,14-17] and full morphology neuron tracing methods [18-21] now make it feasible to map the mammalian whole-brain at single cell resolution [22-24]. Large international efforts such as the BRAIN Initiative Cell Census Network (BICCN) [25], MouseLight project [19], Allen Mouse Brain Connectivity Atlas [26] and Mouse Connectome project [27-29], are engaged in cell typing, mapping long-range axonal projection and microcircuit connection analyses. Massive image datasets are acquired through a variety of high-resolution, high-throughput imaging techniques, such as serial two-photon tomography (STPT), fluorescence micro-optical sectioning tomography (fMOST), light-sheet fluorescence microscopy (LSFM), volumetric imaging with synchronous on-the-fly-scan and readout (VISoR).

A critical technique required to use these data is registration (alignment) of brains, their compartments, and various neuronal structures including somas, dendrites, and axon arbors. Data that are acquired across subjects, modalities, time or even species must be mapped onto a canonical coordinate space. Its importance is seen in multiple ways. First, registration of datasets of different modalities generated in different projects provides a valuable resource for ever-expanding studies of neuron wiring and functions. Second, the registration to a common standard 'atlas' enables digital delineation and quantification of brain anatomy and neurons' morphology and other attributes such as transcriptomics. Third, registration allows quantitative comparison of features of neurons across samples under different conditions, thus enabling analysis of distinct aspects of neurobiology in a coordinated manner.

Established brain atlases such as the Allen mouse brain atlas (using STPT imaging) [30,31] have helped neurobiologists tremendously to study gene expression patterns, brain anatomy, and neural circuits. With the newly produced whole brain single neuron morphology database (e.g.,

using fMOST imaging in Ref[32]), it is critical to register such data to the Allen brain atlas and at the same time compare with mapped neuron populations from experiments using different imaging modalities. There is therefore a need to develop an effective method to accomplish the cross-modality whole brain registration task.

Despite a number of existing studies on registration of whole brain images within one single imaging modality, including for smaller nervous systems from *C. elegans* [33], fruitfly [34], to zebrafish [35,36], there has been few reported work on well scaled cross-modality registration for prevailing bioimaging methods, especially considering the increasing diversity of intensity, texture, and anatomy of structure imaged. In particular, non-uniform characteristics of brain structures makes it challenging to co-register datasets using a number of existing cross-modality registration tools developed in the medical imaging field [37-39] or tools adapted from off-the-shelf registration toolkits [40-42]. Recently, deep neural networks (DNNs) based methods were proposed to further improve registration efficiency and accuracy [43,44]. Yet, application of DNNs to cross-modality bioimaging registration remains unrealized due to the very large scale of the problem and difficulties in designing effective cross-modality similarity loss functions.

In this study, we developed a Coherent Landmark Mapping (CLM) method that integrates deep learning to attempt reliable cross-modality whole brain registration. With CLM as the core local registration module, a comprehensive registration pipeline, named *mBrainAligner*, was built to facilitate the whole brain mapping of images, as well as their compartments and reconstructed neuronal structures. Our algorithm is distinguished in that it systematically addresses the challenges of cross-modality registration from the underlying framework design, allowing resolution of several previous bottlenecks. In addition, the power of DNNs can also be leveraged under CLM framework to further boost registration accuracy and robustness. We show that mBrainAligner can tackle the challenging registration case of fMOST data to the Allen brain atlas achieving dramatically improved accuracy, and providing solid foundation for current large-scale single cell full morphology neuron analysis efforts. The generalization and performance of mBrainAligner were also verified in other modalities including VISoR and magnetic resonance imaging (MRI). Using mBrainAligner, we also developed an fMOST-space mouse brain atlas and showcased the utility of our method for analyzing single cell types.

RESULTS

mBrianAligner algorithm and workflow

We designed mBrainAligner to align 3D mouse brain images to the Allen Common Coordinate Framework atlas (CCFv3) (**Fig. 1**), and the method is applicable to multiple imaging modalities. As fMOST has become an increasingly used technique for whole brain morphology, without loss of generality we use fMOST image alignment as a specific example to describe our general cross-modality imaging registration strategy, which maps image voxel data onto a target image. Importantly, mBrainAligner also enables mapping digitally reconstructed dendritic, axonal, and soma distributions to the target space (**Fig. 1f**). In this manner, the distribution of various

neuronal structures at different resolutions, neuron-population, single neuron, or subcellular, can all be mapped into a standard space for direct visualization, comparison and analysis.

The fMOST whole mouse brain images often vary substantially in their voxel intensity, image texture, and brain anatomy (e.g., uneven brain shrinkage) compared to the average template of CCFv3 acquired using STPT (**Fig. 1a**). To address this challenge, we designed three modules in mBrainAligner: (1) image preprocessing and robust point matching based automatic global registration (**Fig. 1b**), (2) a CLM based automatic local registration (**Fig. 1c**), and (3) an optional semi-automatic refinement (**Fig. 1d**). Our approach can also register and map VISoR and MRI to the standard space for analysis (**Fig. 1a-e**). Using mBrainAligner, we also translated the Allen CCFv3 to a "normalized" fMOST space to produce a digital atlas in the fMOST domain (**Fig. 1g**).

Specifically, in an initial step images are preprocessed to match their sizes and overall intensity profiles. In the fMOST example, a subject image is a 3D image stack of whole mouse brain, which has typical volume of 40k x 30k x 10k voxels. The target image used here is the Allen CCFv3 average template. All fMOST images are firstly scaled anisotropically (XYZ multipliers = 64x64x16) to roughly match the size of the target image, followed by contrast enhancement and noise filtering to remove stripe artifacts that were generated during the knife cutting and imaging processes (**Methods, Fig. 1b, Supplementary movie 1**). Next, we extract and match about 1500 subject-target pairs of brain contour points, estimate the optimal affine transform that maximizes the similarity of brains' outer contour, and thus register the global orientation and scale of these brains (**Methods, Fig. 1b, Supplementary Movie 2**). Visual inspection of the global registration results showed that all test images can be successfully aligned, even if some of them differed almost 180 degrees in their original orientations (**Supplementary Movie 2**).

A key advance in mBrainAligner is the robust and accurate nonlinear local registration that warps a subject image to the target via a point-by-point correspondence between two images. As the cross-modality variations in intensity, texture and shape of globally registered brains often remain severe (**Fig. 1b**), a CLM algorithm is used to deform the target landmark-points that obtained via 2.5D corner detector (**Methods**) to fit the subject brain (**Methods, Fig. 1c, Supplementary Movie 3**), so that each landmark and its neighbors in the target image find their best matches as a group in a coherent way. The deformation of landmarks is driven by three complementary features (gradient, histogram of gradient, and segmentation probability) which encode the texture, shape context and semantic information respectively, while regularized by the shape priors embedded in CCFv3 or fMOST atlas. A DNN is used to estimate the segmentation of six main brain regions, including hypothalamus (HY), caudoputamen (CP), hippocampal formation (HPF), cerebral cortex (CTX), cerebellar cortex (CBX) and brain stem (BS), to guide the registration of these areas (**Methods, Supplementary Fig. 1**). Since the landmarks before and after deforming naturally form matching point-pairs, some previous bottlenecks such as the problematic landmark detection across modalities, as well as the non-trivial identification and screening of unreliable matches are intrinsically avoided. Under the CLM framework, the joint efforts of coherent mapping strategy, discriminative feature integration and effective shape prior utilization ensure the robustness and accuracy of mBrainAligner in challenging cross-modality scenarios.

Registration accuracy

We first evaluated mBrainAligner's performance in registering the border of six brain regions of interest, i.e., HY, HPF, CTX, CBX, BS and CP (**Fig. 2b** left), that were annotated by three neuroanatomists independently. The registration quality of mBrainAligner was visually evident for testing images from different modalities including fMOST, VISoR and MRI (**Fig. 2a** and **Supplementary Fig. 2**). Particularly, for 31 fMOST whole mouse brain images, the region-wise median Dice scores achieved by mBrainAligner's local alignment ranges from 0.82 to 0.90 (**Fig. 2b** middle) while the average median Dice scores for all interest brain regions reaches 0.88 (**Fig. 2b** right). We compared mBrainAligner with three recently reported mouse brain registration pipelines MIRACL [42], ClearMap [41] and aMAP [45]. In our tests, mBrainAligner outperformed compared methods in all interest regions (**Fig. 2b** middle), and achieved 0.11 higher average median Dice scores than the second-ranked method (e.g., 0.77 for aMAP) (**Fig. 2b** right). It should be noted that all results were generated by applying automatic local registration upon the same globally registered brains.

The anatomical location of somas is often used as a key feature to assign neuron types [46]. We considered 1708 neurons that were reconstructed from 31 fMOST mouse brains with all somas manually annotated (**Fig. 3a**). These somas distribute mainly in cortex and thalamus. Five brain regions, ventral posteromedial nucleus (VPM), caudoputamen (CP), ventral posterolateral nucleus (VPL), dorsal part of the lateral geniculate complex (LGd) and medial geniculate complex (MG), contain more than 40 somas. We computationally identified the anatomical locations of these somas by mapping them to CCFv3 using mBrainAligner and several alternative registration methods. Compared with the manually annotated soma locations, mBrainAligner achieves the average soma mapping accuracy of 76% for all somas (**Fig. 3b**), which is at least 19% higher than other methods. A similar conclusion can be drawn by taking a closer look at the results of individual brain regions (**Fig. 3d**). For those somas whose locations mismatch between automatic registration and manual annotation, we calculated their shortest distance to the manually assigned region as distance error, and found mBrainAligner achieved an average distance error of 47.86μm for all somas which is half smaller than the second-ranked method (**Fig. 3c**). As two examples, visualization of registered somas in the VPM (in thalamus) and SSp-n (in cortex) shows that mBrainAligner produces much more consistent results with annotators' expectation indicated by how many somas would be correctly mapped into these regions (**Fig. 3e**). We analyzed the distribution of wrongly localized somas (**Fig. 3f, Supplementary Fig. 8**) and observed that most errors occurred in localizing VPL as VPM, which are two adjacent small regions without clear discriminative boundary between them in fMOST imaging (**Fig. 3g**).

It is hypothesized that different thalamic regions have unique cortical projection patterns[47]. We examined this by computationally predicting the axon projections of 63 neurons from six different brains with somas in VPM or VPL. We found their axons terminated predominantly in layers 4 and 6 of cortex and formed clear patterns (**Fig. 3h**). Compared with anatomists' manual annotation, mBrainAligner predicted 89.1% of the projection target regions when automatic local registration was used (**Fig. 3i, Supplementary Fig. 3**). The accuracy was further improved to 96.29%

after semi-automatic registration was applied (**Supplementary Fig. 4d**). For 162 neurons with apical dendrites that distributed in the L1 layer of cortex (**Fig. 3j**), the respective prediction accuracy is more than 90%.

fMOST-domain CCF/atlas

The Allen CCF [30,31] is an increasingly used standard in mouse brain research. This atlas was developed using iteratively averaged STPT TissueCyte imaging. In a similar manner we used mBrainAligner to build the first fMOST-domain atlas of mouse brain (**Methods, Fig. 4a-b, Supplementary Fig. 5**), including an average template (**Fig. 4b** upper-left) and an annotation template (**Fig. 4b** bottom-left), bridging several gaps between fMOST and Allen CCFv3. First, the morphology variation between these two modalities was identified in a quantitative way (**Fig. 4c**). Second, we established a reusable and invariant transformation between the two atlases (**Fig. 4b** bottom-middle), and thus brain region annotation labels and reconstructed results provided in each modality can be effectively shared. Third, we reduced the technical difficulty to directly map images across these two modalities (**Fig. 4d**). The proposed method is generic and can also be used to build other modality-specific atlases when needed.

The robust and accurate registration approach of mBrainAligner ensured the average template required only a small number of samples (36 fMOST whole mouse brains), much fewer than used in the Allen CCFv3 (1675 TissueCyte whole mouse brains), to achieve a similar level sharpness of boundary of brain regions (**Fig. 4a**, **Supplementary Fig. 5**). We then built the fMOST annotation template by backward mapping the annotation of CCFv3 (**Fig. 4b**). In this way, we ensured consistent definition of brain anatomical regions in the two atlases and facilitated the sharing of information across modalities. We also asked independent neuroanatomists to further validate the biological meaningfulness of the fMOST atlas, especially in the motor cortex, a region of recent focus in the US BRAIN's consortium effort [48].

The fMOST-domain atlas also affords improved registration accuracy. Using the same metrics described above, we re-evaluated the performance of mBrainAligner and all other registration methods to register fMOST images to the fMOST atlas. Because the most notable differences of cross-modality anatomy and intensity are no longer present, all metrics, including Dice scores of brain delineation, soma localization accuracy, distance errors of mapped somas, and axon projection prediction, show clear improvements (**Fig. 4d**) with the average distance error of mapped somas is reduced to around 30μm and the Dice score of registered brain regions is improved to be around 0.90.

Cell type analysis enabled by mBrainAligner

To demonstrate the utility of mBrainAligner in cell type analysis, we studied neuronal projection pathways at the single neuron resolution. The topography of thalamic neurons was characterized previously at the neuron population level [49]. Here, we used mBrainAligner to map neurons

reconstructed via our BICCN consortium effort [32] to Allen CCFv3. We identified 1268 cortical axon arbor clusters that projected to the major cortical areas (e.g., SSp-bfd/m/n for VPM neurons) and studied their correlation with soma locations (**Fig. 5a**). Following the convention of CCFv3, larger values of x-, y- and z-dimensions represent more posterior, ventral and medial locations in the 3D brain atlas.

As an illustrative analysis, the cortex was expanded as a 2D top view map and the axon arbor locations were quantified within the map. We found that axon arbors of VPM neurons formed a stripe-shaped distribution, with the longitude approximately aligning with the x-axis. This axis is correlated with the x-axis of soma and anti-correlated with y- and z-axis of soma (**Fig. 5b**). The dominant pattern (*p*-value = 6.5e-79) of VPM topography is that neurons originating in the dorsal VPM project to the posterior part of the primary somatosensory cortex, namely the barrel field (SSp-bfd). This pathway is significantly shorter than the pathway between ventral-VPM and SSp-m (**Fig. 5d**). The z-axis of axon is anti-correlated with the y- and z-axis of soma (**Fig. 5b**). The same relationship was observed between axon and soma locations of VPL neurons, except that their axon z-axis is anti-correlated with soma x-axis (*p*-value = 0.025). The LGd neurons exhibit a 'twisted' arrangement where the x- and z-axis of axon are anti-correlated with the x- and y-axis of soma (**Fig. 5a,d**). Among the four sensory relay nuclei, MG neurons show the lowest level of topography where only the x-axes of soma and axon were correlated (*p*-value = 0.015, **Fig. 5a,d**). Morphological types of axon arbors showed limited level of correlation with soma locations (**Fig. 5b**). For the non-relay thalamic nuclei, especially high order nuclei including VM and RE, we integrated neurons with different nuclei origins and performed an overall topography test (**Fig. 5a,c**). The overall relationship of soma and axon locations is highly consistent with that of VPM and VPL, especially the anterior-posterior arrangement of axon arbors. From anterior-ventral-medial nuclei, such as PT and RH, to posterior-dorsal-lateral nuclei, such as IGL, axon arbors follow an anterior-posterior distribution pattern.

DISCUSSION

Recent large-scale international initiatives have generated an increasingly large set of high-resolution brain images collected across different projects using a variety of imaging, labeling and sample preparation techniques. Joint brain data mining and analysis of these data require a reliable and robust cross-modality registration method. Previous studies have mainly focused on the intra-modality [33-36], or adapted frameworks that were originally designed for medical imaging [40-42]. The immense diversity of intensity, texture and anatomy variations inherent in multi-modality bioimaging often prohibits the utilization of these methods or renders them with limited performance. In particular, for the fMOST images, severe distortion and artifacts are introduced due to fixative perfusion, resin embedding, and imaging.

In this work, we presented mBrainAligner, a cross-modality registration pipeline to fill this computational gap. Our CLM algorithm enables mBrainAligner to tackle the challenge of cross-modality registration systematically. Distinguished from previous methods, CLM establishes a dense correspondence between two images by iteratively deforming the target landmarks to fit

the subject brain. The "coherent" mapping ensures every landmark is matched by incorporating neighborhood information constrained by shape priors embedded in the atlas. It therefore avoids problematic landmark detection and matching due to greatly varying conditions in cross-modality scenarios. By applying corner detector on the CCFv3 annotation template, we guaranteed all target landmarks are located on the boundaries of brain regions defined in the atlas. In this way, the target landmarks naturally capture the shape priors of these regions and can be viewed as a simplified point-set representation of CCFv3 atlas. The smooth and coherent deformation of such a simplified atlas onto a subject brain implicitly utilizes the embedded priors.

Our method is further improved by deep learning. Previously, DNN approaches have achieved great success in biomedical image segmentation [50,51], segmentation-induced registration[52] and intra-modality registration [53,54]. However, cross-modality bioimaging registration remains challenging for DNNs due to the large scale of the problem, the difficulties in generating sufficient training data for supervised networks [55,56] and in designing effective similarity loss function for unsupervised networks [57,58]. CLM bypasses these obstacles by integrating the deep learning-based segmentation probability as one of the discriminative features to drive the deformation of landmarks. We showed that the introduction of deep learning-derived features can effectively boost the registration accuracy of mBrainAligner in terms of both region-wise and brain-wide Dice scores (**Supplementary Fig. 1d,e**). In addition, as we focus on the various anatomical regions in a brain in this study, our method can be iteratively applied to any anatomical regions in future studies if needed, and it can also be used for specific regions to ensure such areas' alignment is as accurate as possible, only limited by the image resolution and computational cost of the optimization.

Motivated in part by the on-going large-scale collaboration of US BRAIN's BICCN program to characterize brain cell types across multiple modalities, we have used mBrainAligner to integrate information of 31 high resolution fMOST images, where tens of hundreds of reconstructed single neuron full morphology were precisely mapped to the CCFv3 atlas. Our effort facilitates the subsequent axon projection analysis and cell typing. For the first time, we analyzed the neuronal projection pathway at the single neuron resolution and suggested a general topographic rule of thalamocortical projection. In addition to what we show in Results, a whole brain map of 3D full neuron morphology generated in this way also helped neurobiologists test a number hypotheses regarding neuronal projection diversity at multiple organizational levels [32].

With mBrainAligner, we generated the first single-cell resolution mouse brain atlas in the fMOST domain. This extends the utility of CCFv3 from neuron population level to the single cell level. Brain atlases have laid solid foundations for many neuroscience studies, and it is essential that the brain atlases keep pace with the advancing of whole brain imaging techniques. As a large amount of fMOST images are being increasingly generated in the field, a single cell resolution atlas in the fMOST domain will be invaluable. However, the atlas building process is computation-costing and labor-consuming. In this work, we very much ease the construction of fMOST atlas with mBrainAligner. The accurate and robust cross-modality registration capability of mBrainAligner enables us to build a "standard" template from a small number of samples with comparable sharpness of anatomical boundary. By precisely registering the fMOST average

template to CCFv3 with mBrainAligner and then back-projecting the annotation of CCFv3 onto fMOST, a smooth transformation of annotations and identical parcellation of brain regions between two atlases are guaranteed.

Finally, for cross-modality image registration, how to quantify the registration accuracy is often debated [59]. Since soma locations, axon projection and neuronal morphology were used as defining features in the task of cell typing [60], in a biologically meaningful way, we show that mBrainAligner produces significantly improved results than alternative approaches. In addition, mBrainAligner is not limited to the intra- and cross-modality mouse brain registration, its utilities can also be extended to the registration of partially imaged brain (**Supplementary Fig. 6**) and multi-timepoint data or other species (unpublished data). We have open-sourced mBrainaligner, as well as some useful tools including 2.5D corner detector, stripe artifacts removal, and image or metadata warping tools, to promote interdisciplinary and reproducible researches. As increasingly large multimodal imaging data sets are generated, approaches such as mBrainAligner will be essential to analyze, manage, and visualize these data.

ACKNOWLEDGMENTS

AUTHOR CONTRIBUTIONS

DECLARATION OF INTERESTS

The authors declare no competing interests.

METHODS

Data preparation

The average and annotation template of CCFv3 were downloaded from Allen Institute web portal (http://atlas.brain-map.org/). The detailed sample preparation, imaging and atlas generation methods have been described in Ref[31]. Since the foreground brain area in CCFv3 average template is close to image boundaries, to eliminate the computational ambiguity, we padded the CCFv3 average template (25μm) by 20 pixels in both ends of anterior-posterior axes and use the padded image as the target.

Our fMOST dataset consisted of 57 brains of male and female transgenic mice (P56), with sparsely labeled cells in cortical, thalamic, claustral, and striatal regions, and for cholinergic, noradrenergic and serotonergic neuronal types. The detailed sample preparation and imaging methods were describe in Ref[32]. The auto-fluorescence channel was used for image registration. We use the

TeraConverter module of Vaa3D[61] to perform image downsampling. The neurons and somas of 31 fMOST brains were reconstructed via TeraVR module[18] of Vaa3D.

The MRI image is from the dataset that the image volumes representing the canonical Waxholm Space (WHS) adult C57BL/6J mouse brain. All volumes are represented at 21.5µm isotropic resolution. The dataset is openly available at https://www.nitrc.org/projects/incfwhsmouse. This dataset includes five images. Three T1-, T2*-, and T2-Weighted MR volumes are generated at the Duke Center for In-Vivo Microscopy, one is the Nissl stained dataset obtained by Drexel University, and one is the manually labeled atlas dataset. The label volume represents phase one delineations of the WHS mouse brain. The atlas contains 26 structures (+ inner ear) in accordance with the NeuroLex Brain Partonomy at: https://scicrunch.org/scicrunch/interlex/dashboard. Here we chose the T2*-weight MRI image dataset as test data, and removed brain tissues that did not match CCFv3 based on the provided manually labeled atlas.

The VISoR dataset was generated from an 8-week-old C57BL/6J mouse. The brain sample was sectioned into 300µm slices, cleared and then stained with DAPI to label the nuclei of all cells. All slices were imaged with a custom VISoR microscope for high-throughput volumetric imaging at 1x1x2.5µm^3 voxel resolution, and stitched together to reconstruct the whole mouse brain volume. The dataset was downsampled to 4x4x4µm^3 resolution before registration.

The LSFM partial brain hippocampus dataset was generated from an 12-week-old Thy1-Yellow Fluorescent Protein (YFP) mouse (strain B6.Cg-Tg(Thy1-YFPH)2Jrs/J nº003782; The Jackson Laboratories). Same sex littermates were group-housed under a 12-h light/dark schedule (lights on at 09:00 a.m.) in controlled environmental conditions of humidity (60%) and temperature (22 ± 2 ºC) with free access to food and water. The mice were sacrificed and transcardially perfused with cold phosphate buffered saline (PBS), followed by cold CLARITY hydrogel solution. The brains were removed from the skull, immersed in 20 mL of hydrogel solution and stored at 4ºC shielded from light. After 2-3 days at 4ºC, hydrogel polymerization was induced by 3h incubation at 37ºC. Contact with oxygen was prevented with a vegetal oil layer. Thereafter, the already polymerized surrounding hydrogel was removed. Entire brains were immersed in 50 mL of clearing solution and stored in a water bath at 45ºC. After 2 months of incubation in clearing solution for passive clearing, optical transparent brains were washed with 50 mL PBST (0.1% TritonX in 1X PBS) twice for 24 hours each, at 45ºC. After that, the samples were immersed in a Refractive Index Matching (RIM; 75 g diatrizoic acid, 70 g d-sorbitol and 23 g n-methyl-d-glucamine in 100 mL of water) medium for 2 days before imaging. After incubation in RIM the samples were imaged in a custom-built Single Plane Illumination Microscopy (SPIM) set-up available at the Mesoscopic Imaging Facility of EMBL Barcelona (https://www.embl.es/services/mesoscopic-imaging-facility/). We used detection lens with magnification 5x, a laser wavelength of 488 for fluorescence excitation and a 5µm z step, obtaining a 1.29x1.29x5µm^3 voxel size.

All experiments related to the use of mice followed NIH guidelines, and received approval from the Institutional Animal Care and Use Committee of respective institutions.

Removal of stripe artifact

The stripe noise present in the raw fMOST images is mainly caused by fluorescent bleaching during the knife cutting and imaging process. We modeled this kind of stripe artifacts as multiplicative periodic noise to approximate its imaging nature and designed a log-space frequency notch filter to realize the high-quality stripe artifacts removal (**Supplementary Movie 1**). For each fMOST image, (1) One 2D coronal slice with the largest foreground brain area was extracted (**Supplementary Fig. 7a**) and converted to the frequency domain using Fast Fourier Transform (FFT) (**Supplementary Fig. 7b**). (2) By examining the frequency spectrum, the band width, orientation, and cutoff frequency of the notch filter were identified and then used to construct a Gaussian notch filter (**Supplementary Fig. 7c**). (3) We imposed the log transform on the intensity of fMOST image in the spatial domain to convert the multiplicative noise to additive one (**Supplementary Fig. 7d**). (4) The log-transformed fMOST image was filtered in the frequency domain in a slice-by-slice manner using the Gaussian notch filter generated in step 2 (**Supplementary Fig. 7e**). (5) Finally, we computed the inverse FFT on the filtered spectrum and used inverse-log transform to bring the filtered image back from the log space (**Supplementary Fig. 7f**).

Robust point matching based automatic global registration

To minimize the impact of intensity variation between different modalities, we implement the automatic global alignment by affine aligning brains' outer-contour points through point-set matching. First, the foreground brain region was extracted via Otsu thresholding[62], followed by morphology filtering to remove the small and thin artifacts. Then we uniformly sampled (7x7x7 grid) the contour of the foreground region to obtain a dense point-set (~1500 points per brain) that represents the shape of brain's outer-contour. To tackle the large direction variation between brains, the principal axes of target and subject point-sets were extracted using principal component analysis (PCA), and then rigidly aligned. Finally, following the deterministic annealing framework of robust point matching[63], we iteratively refine the scaling, translation, rotation, and shearing of subject point-set to maximize its shape similarity to the target one (**Supplementary movie 2**). We set the initial annealing temperature to 0.25, and gradually decrease the temperature with an annealing rate of 0.96 during iteration.

2.5D corner detection

Since CLM establishes the correspondence between two brains by deforming the landmarks defined in target brain to fit the subject brain, the quantity and quality of target landmarks will have a big impact on the overall performance of registration. We designed a 2.5D corner detector to automatically extract points of high curvature (corners or junction of different brain regions) of a 3D image, and applied it on the annotation template of CCFv3 to generate anatomical significant target landmarks. We realized the 2.5D corner detector via a two-level detection and screening strategy.

In the first level, given a 3D image, we started out by extracting all its coronal, sagittal, and horizontal planes. For each plane, the Harris response[64] of each pixel was computed, thresholded

(0.1), and non-maximum suppressed (with window size 7x7) to find the local maxima as candidate corners. We denoted these candidate corners as the first-level corners, and saved their Harris responses at coronal, sagittal and horizontal planes respectively for the second-level screening.

In the second level, we screened the first-level corners by only retaining ones that were detected as first-level corners in at least two of the three orthogonal planes. We called remained corners second-level ones and updated their Harris response by accumulating their responses at corresponding orthogonal directions. The final landmarks were obtained by applying 3D non-maximum suppression (with windows size 31x31x31) on the second-level corners. The quantity of corners can be controlled by choosing different window sizes of non-maximum suppression.

Coherent landmark mapping (CLM) based automatic local registration

Coherent landmark mapping (CLM)

To maximize the robustness of cross-modality registration, we designed a novel CLM algorithm to iteratively deform the target landmarks to fit the subject brain (**Supplementary Movie 3**). The landmarks before and after deforming naturally establish the correspondence between two images, and were used to calculate the displacement field for local image warping. CLM based the landmark deforming upon an integration of three discriminative features described in the next section to enhance the robustness and accuracy of the algorithm in tackling the challenge of cross-modality registration. In addition, under the CLM framework, the priors such as spatial relationship and shape of brain regions were readily integrated and utilized in the coherent deforming process.

Suppose we have a subject image that consists of N voxels $V=\{v_i, i=1,2,...,N\}$, and a target landmark-set of M points $L=\{l_j, j=1,2,...,M\}$, where v_i is the *i*-th voxel and l_j is the *j*-th landmark in subject and target image respectively. Let $P=\{p_{ij}, p_{ij}\in[0,1]\}$ be the classification probability of *i*-th voxel to the *j*-th landmark, we form the CLM as the following energy minimization problem:

$$E(P,\Theta)=\sum_{j=1}^{M}\sum_{i=1}^{N} p_{ij}(1-s_{ij})\frac{\left\|v_i-f(l_j,\Theta)\right\|^2}{r^2}+T\sum_{j=1}^{M}\sum_{i=1}^{N} p_{ij}\log p_{ij},\qquad s.t.\sum_{i=1}^{N} p_{ij}=1 \tag{1}$$

where $f(l_j,\Theta)$ is the spatial transform which maps the landmark l_j to a new location with parameters Θ, $s_{ij}\in[0,1]$ denotes the matching score between voxel v_i and currently deformed landmark $f(l_j,\Theta)$, and r is the distance influence factor which controls the impact of voxel-to-landmark distance to their classification probability. Minimizing the first term encourages assigning larger classification probability to the voxel-to-landmark pair with higher matching score and smaller Euclidian distance. While minimizing the second term is equivalent to maximizing the entropy of P, which aims to enforce the convexity of the energy function and

alleviate the risk of algorithm getting trapped in the local minimum during optimization. T acts as a balance factor between two terms.

We adopted a dual update strategy to solve the joint classification and spatial transform optimization problem posed in energy function (1). In each iteration, we first fixed the transformation Θ and calculate the voxel-to-landmark classification P with currently deformed landmarks, then update the transform and perform landmark deformation with classification probability fixed. We denote the above two steps as *landmark guided voxel classification* and *voxel classification guided landmark deformation* respectively.

Landmark guided voxel classification. Given spatial transform Θ, the deformed target landmarks can be obtained as $f(L,\Theta)$. For any i, j value, minimizing $E(P,\Theta)$ respect to P will lead to:

$$\frac{\partial E}{\partial p_{ij}} = 0 \Rightarrow p_{ij} = \exp\left(-\frac{(1-s_{ij})\left\| v_i - f(l_j,\Theta)\right\|^2}{r^2 T} - 1 \right) \quad (2)$$

we choose $T=1$, and normalize classification probability so that $\sum_i p_{ij} = 1$ for any $i \in [0, N]$ once they are updated using equation (2). To speed-up the iterative voxel classification, we only concern a subdomain (21*21*21) around each landmark and choose $r=10$.

Voxel classification guided landmark deformation. With fixed voxel classification probability P, we realized the coherent landmark deforming in three steps. First, we preliminarily updated each landmark to the weighted center of mass of all voxels $l_j^{pre} = \sum_{i=1}^{N} p_{ij} v_i$. Then we updated transform parameters Θ so that deformed landmarks $f(L,\Theta)$ can best approximate their preliminary updated ones $\{l_j^{pre},\ j = 1,2,...,M\}$ under certain smoothness and brain shape prior constraints. We choose smooth-thin-plate-spline (STPS)[65] to model the spatial transform f with parameters Θ, which can be decomposed into an affine transform and a smoothness parameter λ regularized non-linear non-affine warping component. If $\lambda=0$, an exact interpolation was performed. We choose $\lambda=0.001$ to balance the goodness of fit between two point-sets and the smoothness of deformation. The spatial transform parameters Θ were solved as a least-squares solution of STPS. Finally, we performed STPS transformation with updated parameters on initial target landmarks to realize the coherent landmark deforming. Since target landmarks encapsulate the shape priors of CCFv3, and their deformation smoothness is regularized by STPS during iterative mapping, thus guarantees the effective utilization of shape priors.

If provided, the modality-specific shape priors can also be accommodated under the CLM framework to further enhance the robustness and accuracy of registration. Given fMOST atlas, since the transformation between CCFv3 and fMOST atlas was known and fixed, we utilized this modality-specific shape priors by first mapping the initial landmarks of different brain regions to fMOST space, and then deforming them in a region-wise manner following the above mentioned STPS deforming strategy. In our implementation, this region-wise constraint was applied before the brain-wise constraint during each iteration.

This iterative fix-and-update strategy is similar to the expectation-maximization (EM) optimization, we stop the iteration until the average of displacement of landmarks between adjacent iterations is below a given threshold.

Matching score computation

We based the calculation of matching score between voxel-to-landmark pairs upon three complementary features: (i) gradient, (ii) histogram of oriented gradients (HOG)[66], and (iii) deep-learning based segmentation probability. The gradient feature was generated by applying a Sobel filter (3x3x3) on Gaussian smoothed (3x3x3) volume. At a given location, its HOG feature was calculated by concatenating the normalized gradient histograms of 8 blocks within the patch (21x21x21) that centered on that location. We divided each patch into 27 cells (7x7x7) and combined its neighboring 2x2x2 cells to create blocks. For each block, the gradient histogram (9 orientations) of each cell within it was computed, concatenated and normalized to form the block feature. This resulted in a 576 dimensional HOG feature for each location. As a proof of principle, we adopted a simplified 3D U-Net[67] to generate the segmentation probability (0~1) of each voxel to six main brain regions (HY, HPF, CTX, CBX, BS, CP) and background. Indeed, other more sophisticated segmentation networks can be readily adopted under the CLM framework to further improve the registration performance. The network architecture used in this study is shown in **Supplementary Fig. 1a**, which contains a classical encoder-decoder structure. Considering the relatively small training dataset, we use four layers at the encoder stage and four layers at the decoder stage, and they have 32, 64, 128 and 256 channels respectively. The 7-dimensional score maps output by the final softmax layers were used as the segmentation probability feature. The network was trained from scratch on 57 brains with ground truth segmentation labels obtained via mBrainAligner. We used 23 brains as the training set, 3 brains as the validation set and the remaining for testing. The segmentation results of six brain regions are visualized in **Supplementary Fig. 1c** with their segmentation accuracies shown in **Supplementary Fig. 1b**. The benefit of DNN to mBrainAligner was illustrated in **Supplementary Fig. 1d,e.**

Finally, we computed the matching score of each landmark-to-voxel pair by accumulating the similarity score of their centered patches (21x21x21) upon three feature maps. In our implementation, (i) inverse mean squared error, (ii) mutual information, and (ii) normalized cross-correlation were used as similarity metrics.

Semi-automatic refinement

The semi-automatic registration module provides an easy-to-use interactive interface for investigators to examine and fine-tune the registration results (**Supplementary Fig. 4a**). In this interface, the boundary of brain regions defined in CCFv3 was vectorized as Bezier curves and visualized as an overlaid layer on the registered brain and CCFv3 average template respectively. The registration quality can be examined by checking how well the registered brain fits the CCFv3 in the coronal, sagittal and horizontal view at different scales. Since the Bezier curves were

defined by a series of control nodes, it is possible to change the point correspondence by dragging the boundary curves in three-view panels to fine-tune the alignment (**Supplementary Movie 4**) with results compatible with the automatic registration.

The boundary curves can be adjusted independently or coherently with different smoothness and influence range by tuning parameters in the right panel of interface. In addition to manual adjustment, this module also provids a magnetic lasso mode to assist in the adjustment of the curves in a semi-automatic manner, which can greatly improve the efficiency and accuracy of fine-tuning at areas with clear boundaries (**Supplementary Movie 4**). We demonstrated that the semi-automatic registration module can also be used to register damaged or partially imaged brains (**Supplementary Fig. 6**), which usually can hardly be registered using fully automatic methods.

3D fMOST atlas building of mouse brain

We built the fMOST average template from 36 mouse brains in an iterative way. Before entering the iteration, all fMOST brains were preprocessed and globally aligned to CCFv3 following the methods described above. To encourage a symmetric atlas, the globally aligned brains were mirrored across the midline, which resulted in a total of 72 brains. We iterated the following two steps until converge, (i) each brain was locally registered to the template (we chose a high-quality fMOST brain as the template in the first iteration) by using the automatic local registration module of mBrainAligner and averaged together; (ii) the average deformation field over all brains was computed, inverted, and used to perform shape normalization on the average image obtained in (i). This shape-normalized average brain was then used as the anatomical template in step (i) for the next iteration. We stopped the iteration until the sum of the magnitude of average deformation field was below a certain threshold.

We generated the fMOST annotation template by first aligning the fMOST average template to CCFv3 and then back projecting the annotation template of CCFv3 using the inverse of deformation field generated. To ensure a highly accurate registration, we registered the fMOST average template to CCFv3 by concatenating the automatic and semi-automatic registration module of mBrainAligner.

Data availability

The whole brain image and registered image datasets are released under BICCN's Brain Image Library (BIL) at Pittsburgh Supercomputing Center (www.brainimagelibrary.org).

Code availability

The source code of all mBrainAligner modules, including stripe artifacts removal, automatic global registration, automatic local registration and semi-automatic refinement can be found at Vaa3D's GitHub page (https://github.com/Vaa3D/vaa3d_tools/tree/master/hackathon/mBrainAligner).

References

1. Gong, H., *et al.* High-throughput dual-colour precision imaging for brain-wide connectome with cytoarchitectonic landmarks at the cellular level. *Nature communications* **7**, 1-12 (2016).
2. Economo, M.N., *et al.* A platform for brain-wide imaging and reconstruction of individual neurons. *Elife* **5**, e10566 (2015).
3. Osten, P. & Margrie, T.W. Mapping brain circuitry with a light microscope. *Nature methods* **10**, 515-523 (2013).
4. Ragan, T., *et al.* Serial two-photon tomography for automated ex vivo mouse brain imaging. *Nature Methods* **9**, 255-258 (2012).
5. Wang, H., *et al.* Scalable volumetric imaging for ultrahigh-speed brain mapping at synaptic resolution. *National Science Review* **6**, 982-992 (2019).
6. Xu, F., *et al.* High-throughput whole-brain mapping of rhesus monkey at micron resolution. *bioRxiv* (2020).
7. Chung, K., Wallace, J., Kim, S.Y., Kalyanasundaram, S. & Deisseroth, K. Structural and molecular interrogation of intact biological systems. *Nature* **497**, 332-337 (2013).
8. Tomer, R., Ye, L., Hsueh, B. & Deisseroth, K. Advanced CLARITY for rapid and high-resolution imaging of intact tissues. *Nature Protocols* **9**, 1682 (2014).
9. Murray, E., *et al.* Simple, scalable proteomic imaging for high-dimensional profiling of intact systems. *Cell* **163**, 1500-1514 (2015).
10. Renier, N., *et al.* iDISCO: a simple, rapid method to immunolabel large tissue samples for volume imaging. *Cell* **159**, 896-910 (2014).
11. Pan, C., *et al.* Shrinkage-mediated imaging of entire organs and organisms using uDISCO. *Nature methods* **13**, 859-867 (2016).
12. Susaki, E.A., *et al.* Advanced CUBIC protocols for whole-brain and whole-body clearing and imaging. *Nature protocols* **10**, 1709 (2015).
13. Richardson, D.S. & Lichtman, J.W. Clarifying tissue clearing. *Cell* **162**, 246-257 (2015).
14. Thomas, R., Smallwood, P.M., John, W., Jeremy, N. & Eshel, B.J. Genetically-Directed, Cell Type-Specific Sparse Labeling for the Analysis of Neuronal Morphology. *Plos One* **3**, e4099 (2008).
15. Aransay, A., Rodríguez-López, C., García-Amado, M., Clascá, F. & Prensa, L. Long-range projection neurons of the mouse ventral tegmental area: a single-cell axon tracing analysis. *Frontiers in neuroanatomy* **9**, 59 (2015).
16. Ghosh, S., *et al.* Sensory maps in the olfactory cortex defined by long-range viral tracing of single neurons. *Nature* **472**, 217-220 (2011).
17. Lin, R., *et al.* Cell-type-specific and projection-specific brain-wide reconstruction of single neurons. *Nature methods* **15**, 1033-1036 (2018).
18. Wang, Y., *et al.* TeraVR empowers precise reconstruction of complete 3-D neuronal morphology in the whole brain. *Nature Communications* **10**, 3474 (2019).
19. Winnubst, J., *et al.* Reconstruction of 1,000 projection neurons reveals new cell types and organization of long-range connectivity in the mouse brain. *Cell* **179**, 268-281. e213 (2019).

20. Zhou, H.*, et al.* GTree: an Open-source Tool for Dense Reconstruction of Brain-wide Neuronal Population. *Neuroinformatics*, 1-13 (2020).
21. Peng, H.*, et al.* BigNeuron: large-scale 3D neuron reconstruction from optical microscopy images. *Neuron* **87**, 252-256 (2015).
22. Kim, Y.*, et al.* Mapping social behavior-induced brain activation at cellular resolution in the mouse. *Cell reports* **10**, 292-305 (2015).
23. Batiuk, M.Y.*, et al.* Identification of region-specific astrocyte subtypes at single cell resolution. *Nature communications* **11**, 1-15 (2020).
24. Ueda, H.R., Dodt, H.U., Osten, P., Economo, M.N. & Keller, P.J. Whole-Brain Profiling of Cells and Circuits in Mammals by Tissue Clearing and Light-Sheet Microscopy. *Neuron* **106**, 369-387 (2020).
25. Ecker, J.R.*, et al.* The BRAIN Initiative Cell Census Consortium: Lessons Learned toward Generating a Comprehensive Brain Cell Atlas. *Neuron* **96**, 542 (2017).
26. Oh, S.W.*, et al.* A mesoscale connectome of the mouse brain. *Nature* **508**, 207-214 (2014).
27. Zingg, B., Hintiryan, H., Gou, L., Song, M.Y. & Dong, H.-W. Neural Networks of the Mouse Neocortex. *Cell* **156**, 1096-1111 (2014).
28. Hintiryan, H.*, et al.* The mouse cortico-striatal projectome. *Nature neuroscience* **19**, 1100-1114 (2016).
29. Bienkowski, M.S.*, et al.* Integration of gene expression and brain-wide connectivity reveals the multiscale organization of mouse hippocampal networks. *Nature neuroscience* **21**, 1628-1643 (2018).
30. Dong, H.W. *The Allen reference atlas: A digital color brain atlas of the C57Bl/6J male mouse*, (John Wiley & Sons Inc, 2008).
31. Wang, Q.*, et al.* The Allen mouse brain common coordinate framework: a 3D reference atlas. *Cell* **181**, 936-953. e920 (2020).
32. Peng, H.*, et al.* Brain-wide single neuron reconstruction reveals morphological diversity in molecularly defined striatal, thalamic, cortical and claustral neuron types. *bioRxiv*, 675280 (2020).
33. Long, F., Peng, H., Liu, X., Kim, S.K. & Myers, E. A 3D digital atlas of C. elegans and its application to single-cell analyses. *Nature methods* **6**, 667-672 (2009).
34. Peng, H.*, et al.* BrainAligner: 3D registration atlases of Drosophila brains. *Nature Methods* **8**, 493-500 (2011).
35. Randlett, O.*, et al.* Whole-brain activity mapping onto a zebrafish brain atlas. *Nature methods* **12**, 1039-1046 (2015).
36. Griffiths, V.A.*, et al.* Real-time 3D movement correction for two-photon imaging in behaving animals. *Nature methods* **17**, 741-748 (2020).
37. Avants, B.B., Tustison, N. & Song, G. Advanced normalization tools (ANTS). *Or Insight* **1–35**(2008).
38. Klein, S., Staring, M., Murphy, K., Viergever, M.A. & Pluim, J.P.W. Elastix: A Toolbox for Intensity-Based Medical Image Registration. *IEEE Transactions on Medical Imaging* **29**, 196-205 (2009).
39. Modat, M.*, et al.* Fast free-form deformation using graphics processing units. *Computer Methods & Programs in Biomedicine* **98**, 278-284 (2010).

40. Niedworok, C.J.*, et al.* aMAP is a validated pipeline for registration and segmentation of high-resolution mouse brain data. *Nature Communications* **7**, 11879 (2016).
41. Renier, N.*, et al.* Mapping of brain activity by automated volume analysis of immediate early genes. *Cell* **165**, 1789-1802 (2016).
42. Goubran, M.*, et al.* Multimodal image registration and connectivity analysis for integration of connectomic data from microscopy to MRI. *Nature communications* **10**, 1-17 (2019).
43. Fan, J., Cao, X., Yap, P.T. & Shen, D. BIRNet: Brain Image Registration Using Dual-Supervised Fully Convolutional Networks. *Medical Image Analysis* **54**(2018).
44. Cao, X.*, et al.* Deformable image registration based on similarity-steered CNN regression. in *International Conference on Medical Image Computing and Computer-Assisted Intervention* 300-308 (Springer, 2017).
45. Niedworok, C.J.*, et al.* aMAP is a validated pipeline for registration and segmentation of high-resolution mouse brain data. *Nature communications* **7**, 1-9 (2016).
46. Zeng, H. & Sanes, J.R. Neuronal cell-type classification: challenges, opportunities and the path forward. *Nat Rev Neurosci* **18**, 530-546 (2017).
47. Harris, J.A.*, et al.* Hierarchical organization of cortical and thalamic connectivity. *Nature* **575**, 195-202 (2019).
48. Muñoz-Castaneda, R.*, et al.* Cellular Anatomy of the Mouse Primary Motor Cortex. *bioRxiv* (2020).
49. Jones, E.G. *The thalamus*, (Springer Science & Business Media, 2012).
50. Seo, H., Huang, C., Bassenne, M., Xiao, R. & Xing, L. Modified U-Net (mU-Net) with incorporation of object-dependent high level features for improved liver and liver-tumor segmentation in CT images. *IEEE transactions on medical imaging* **39**, 1316-1325 (2019).
51. Gu, R.*, et al.* CA-Net: Comprehensive Attention Convolutional Neural Networks for Explainable Medical Image Segmentation. (2020).
52. Iqbal, A., Khan, R. & Karayannis, T. Developing a brain atlas through deep learning. *Nature Machine Intelligence* **1**, 277-287 (2019).
53. Wang, C.*, et al.* FIRE: unsupervised bi-directional inter-modality registration using deep networks. *arXiv preprint arXiv:1907.05062* (2019).
54. Masoumi, N., Xiao, Y. & Rivaz, H. ARENA: Inter-modality affine registration using evolutionary strategy. *International Journal of Computer Assisted Radiology & Surgery* **14**(2018).
55. Xiao, Y., Kwitt, R., Styned, M. & Niethammer, M. Quicksilver: Fast Predictive Image Registration – a Deep Learning Approach. *Other* **158**(2017).
56. Rohé, M.-M., Datar, M., Heimann, T., Sermesant, M. & Pennec, X. SVF-Net: Learning Deformable Image Registration Using Shape Matching. in *International Conference on Medical Image Computing and Computer-Assisted Intervention* (2017).
57. Balakrishnan, G., Zhao, A., Sabuncu, M.R., Guttag, J. & Dalca, A.V. VoxelMorph: A Learning Framework for Deformable Medical Image Registration. *IEEE Transactions on Medical Imaging*, 1788-1800 (2019).
58. Krebs, J., E Delingette, H., Mailhe, B., Ayache, N. & Mansi, T. Learning a Probabilistic Model for Diffeomorphic Registration. *IEEE Transactions on Medical Imaging*, 1-1 (2019).

59. Tward, D.J.*, et al.* Solving the where problem in neuroanatomy: a generative framework with learned mappings to register multimodal, incomplete data into a reference brain. *bioRxiv* (2020).
60. Ramon y Cajal, S. Histologie du système nerveux de l'homme et des vertébrés. *Maloine, Paris* **2**, 153-173 (1911).
61. Peng, H., Ruan, Z., Long, F., Simpson, J.H. & Myers, E.W. V3D enables real-time 3D visualization and quantitative analysis of large-scale biological image data sets. *Nature Biotechnology* **28**, 348-353 (2010).
62. Otsu, N. A Threshold Selection Method from Gray-Level Histograms. *IEEE Transactions on Systems Man & Cybernetics* **9**, 62-66 (2007).
63. HL, C. & Rangarajan, A. A new point matching algorithm for non-rigid registration. *Computer Vision & Image Understanding* **89**, 114-141 (2003).
64. Harris, C.G. & Stephens, M. A combined corner and edge detector. in *Alvey vision conference*, Vol. 15 10-5244 (Citeseer, 1988).
65. Wahba, G. *Spline models for observational data*, (SIAM, 1990).
66. Dalal, N. & Triggs, B. Histograms of oriented gradients for human detection. in *computer society conference on computer vision and pattern recognition* Vol. 1 886-893 (IEEE, 2005).
67. Çiçek, Ö., Abdulkadir, A., Lienkamp, S.S., Brox, T. & Ronneberger, O. 3D U-Net: learning dense volumetric segmentation from sparse annotation. in *International conference on medical image computing and computer-assisted intervention* 424-432 (Springer, 2016).

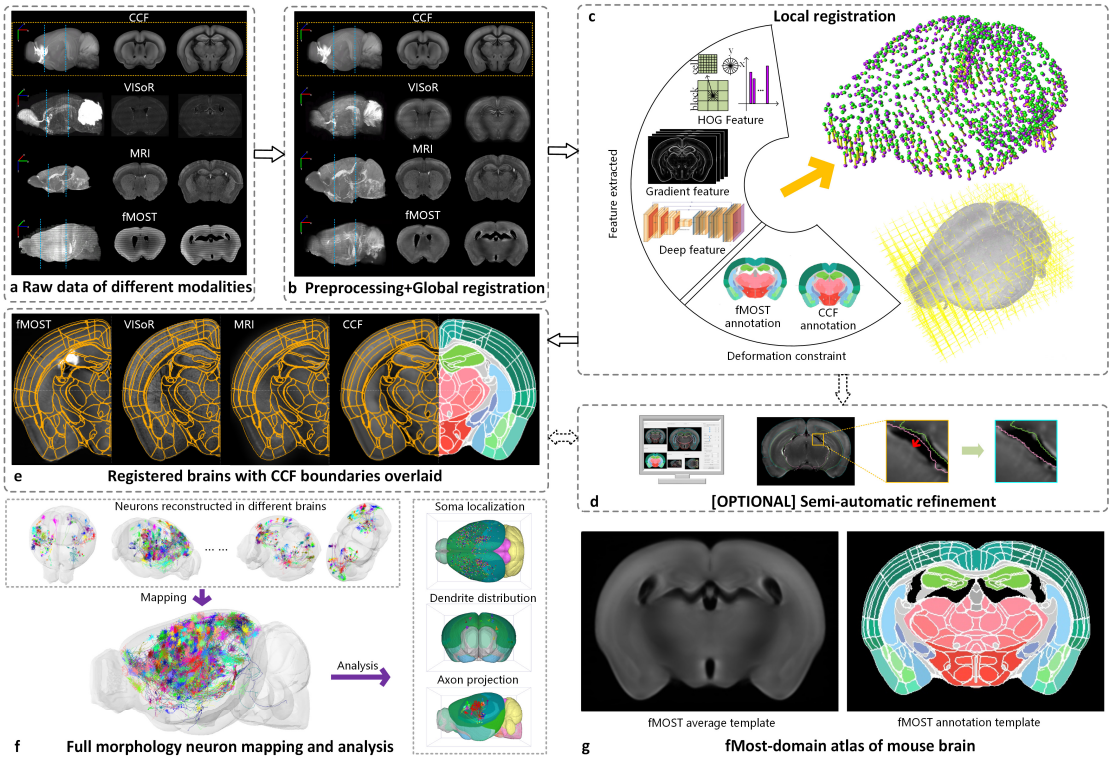

Fig.1| Overview of mBrainAligner for cross-modality image registration, brain delineation, whole brain full morphology neuron mapping, and fMOST mouse brain atlas building. (a) Mouse brain of different modalities exhibit substantial fluctuation in their voxel intensity, image texture, and brain anatomy. The left column shows the maximum intensity projection (MIP) of original brain images of different modalities, two of their coronal slices are shown on the right. (b) Preprocessed and globally aligned brains. For fMOST images, the stripe artifacts were removed before applying global registration. (c) Coherent Landmark Mapping (CLM) based local registration establishes a dense point-by-point correspondence between two images by deforming the target landmarks to fit the subject brains. The landmark deforming is driven by three complementary features (gradient, HOG and deep-learning-derived features) which encode the texture, shape context and semantic information respectively, and constrained by shape priors embedded in atlases. (d) As an optional step, the registration results can be examined and fine-tuned in semi-automatic registration module. (e) Registered brains of different modalities with brain region boundaries defined in CCFv3 overlaid. (f) mBrainAligner enables the mapping of dendritic, axonal, and soma distributions into to a canonical coordinate space for visualization, comparison and analysis. (g) fMOST-domain atlas of mouse brain built with mBrainAligner.

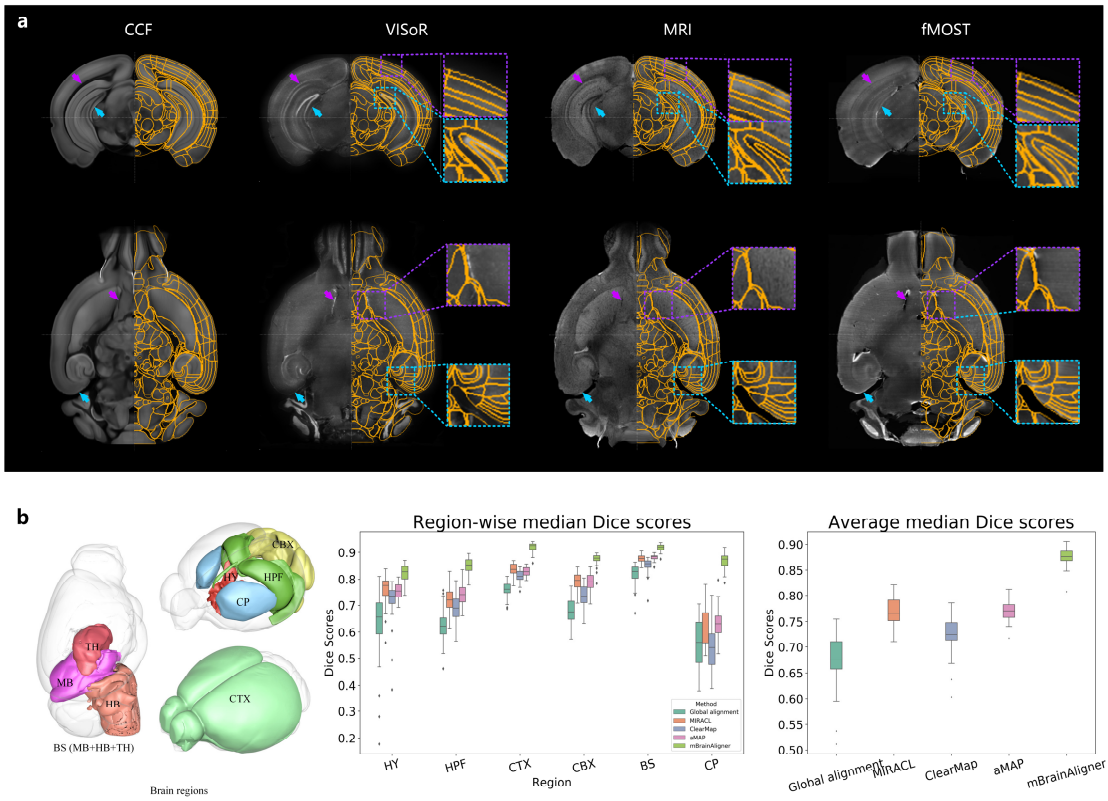

Fig.2| Accuracy of mBrainAligner in brain delineation.

(a) Registered brains of different modalities with brain region boundaries (orange) defined in CCFv3 overlaid. The first and second rows show the coronal and sagittal view of registered brains respectively with zoom-in view of two subregions. The purple and cyan arrows in the first and second rows point to the same spatial coordinates respectively. (b) Quantitative evaluation of registration accuracy of different methods in terms of region-wise and average median Dice scores. The left subpanel shows six brain regions of interest that were annotated by neuroanatomists and used for quantifying the registration accuracy. The middle subpanel shows the region-wise median Dice scores and the right subpanel shows the average median Dice scores of different methods. Box plot: center line, median; box limits, upper and lower quartiles; whiskers, 1.5 x interquartile range; points, outliers;

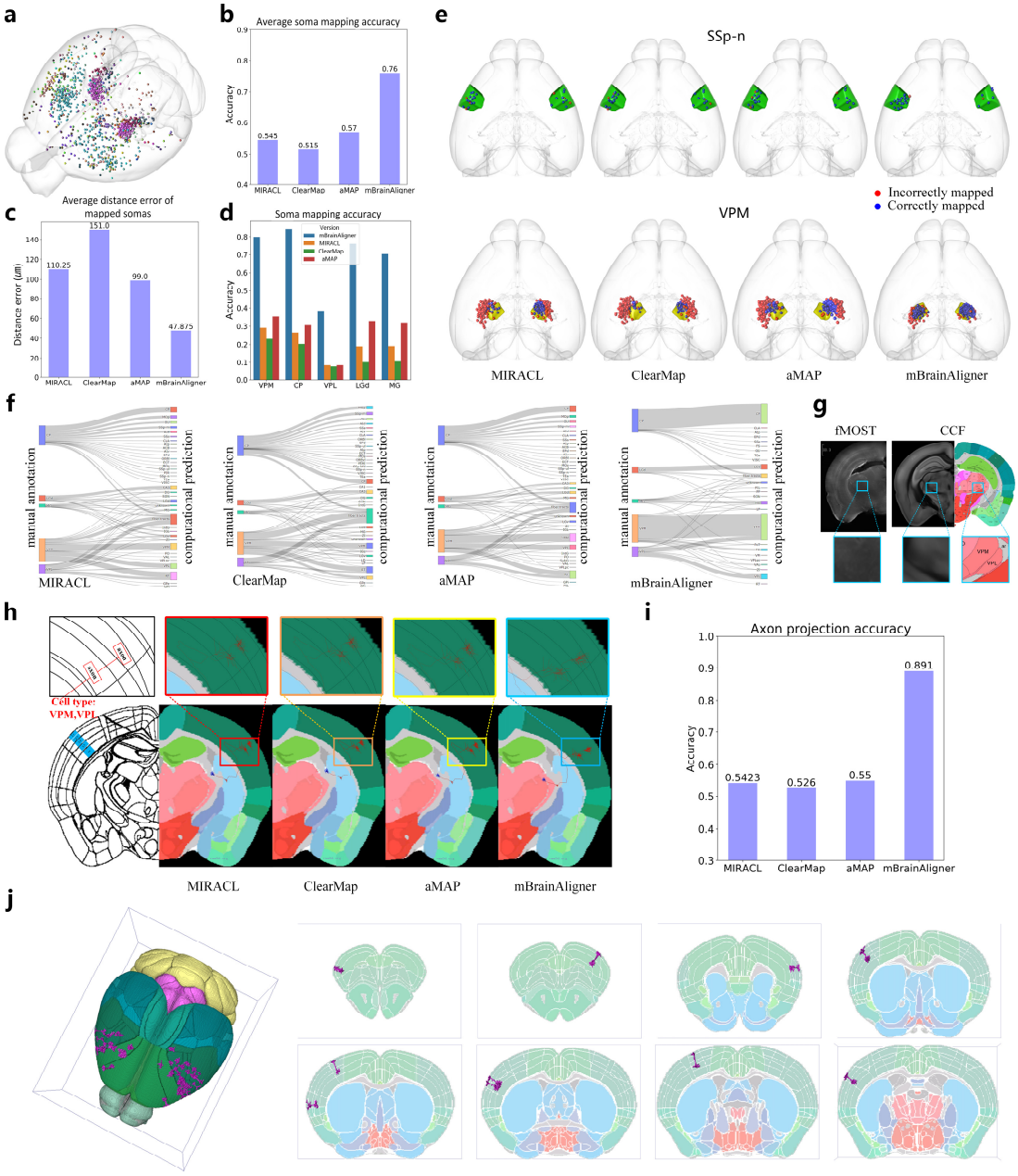

Fig.3| Accuracy of mBrainAligner in computational soma anatomical localizing and axon projection prediction.

(a) Distribution of 1708 somas reconstructed from 31 fMOST brains. Different colors represent different brain regions they were manually annotated. (b) Soma mapping accuracy of different methods (MIRACL, ClearMap, aMAP and mBrainAligner). (c) Average distance error of mapped somas of different methods. (d) Comparison of soma mapping accuracy of different methods in five brain regions (VPM, CP, VPL, LGd and MG). (e) Visualization of mapped somas in two brain regions (SSp-n, VPM). The somas that were mapped outside of their manually annotated region are shown as red dots. Blue dots indicate the correctly mapped ones. (f) Distribution of computational soma localizing results generated by different methods. The left side of diagram shows manually annotated results, and right side shows their computationally predicted results. (g) Zoom-in view of two adjacent small regions (VPM and VPL) where most localization errors occurred. (h) Visualization of axon mapping results of different methods. (i) Computational prediction accuracy of axon projection of different methods on 63 neurons with somas in VPM and VPL. (j) Registered results of 162 neurons with apical dendrites distributed in the L1 layer of cortex. The left-most subpanel visualizes the distribution of neurons in cortex, and other subpanels show the coronal slices with registered apical dendrites overlaid.

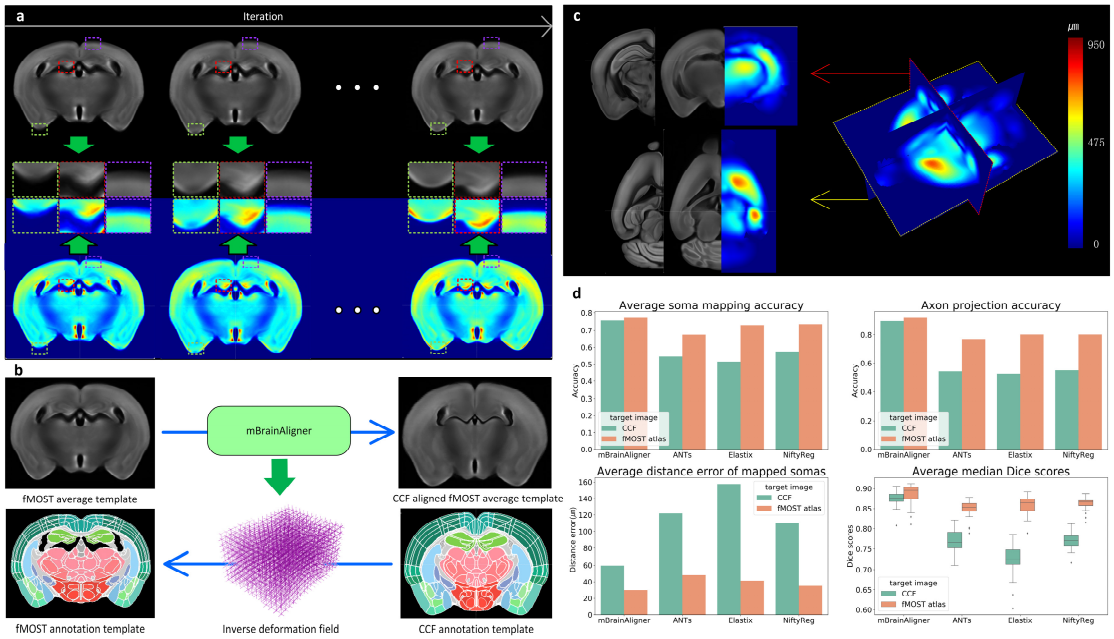

Fig.4| fMOST-domain atlas of mouse brain.

(a) Evolution of fMOST average template in the building process. Left to right show results (coronal plane) generated in the 1st, 2rd, and 7th iteration respectively. The top row and bottom row show the gray-scale and color-code visualized atlas, and the close-up views in middle show the sharpness of average template during iteration. (b) Generation of fMOST annotation template. The fMOST average template was first registered to CCFv3 via mBrainAligner. Then, the fMOST annotation template was generated by backward projecting the annotation of CCFv3 using the same warping parameters for image registration. (c) Visualization of anatomical variation between fMOST and CCFv3 atlas. (d) Re-evaluation of registration accuracy of different methods by registering fMOST data to the fMOST atlas. Box plot: center line, median; box limits, upper and lower quartiles; whiskers, 1.5 x interquartile range; points, outliers;

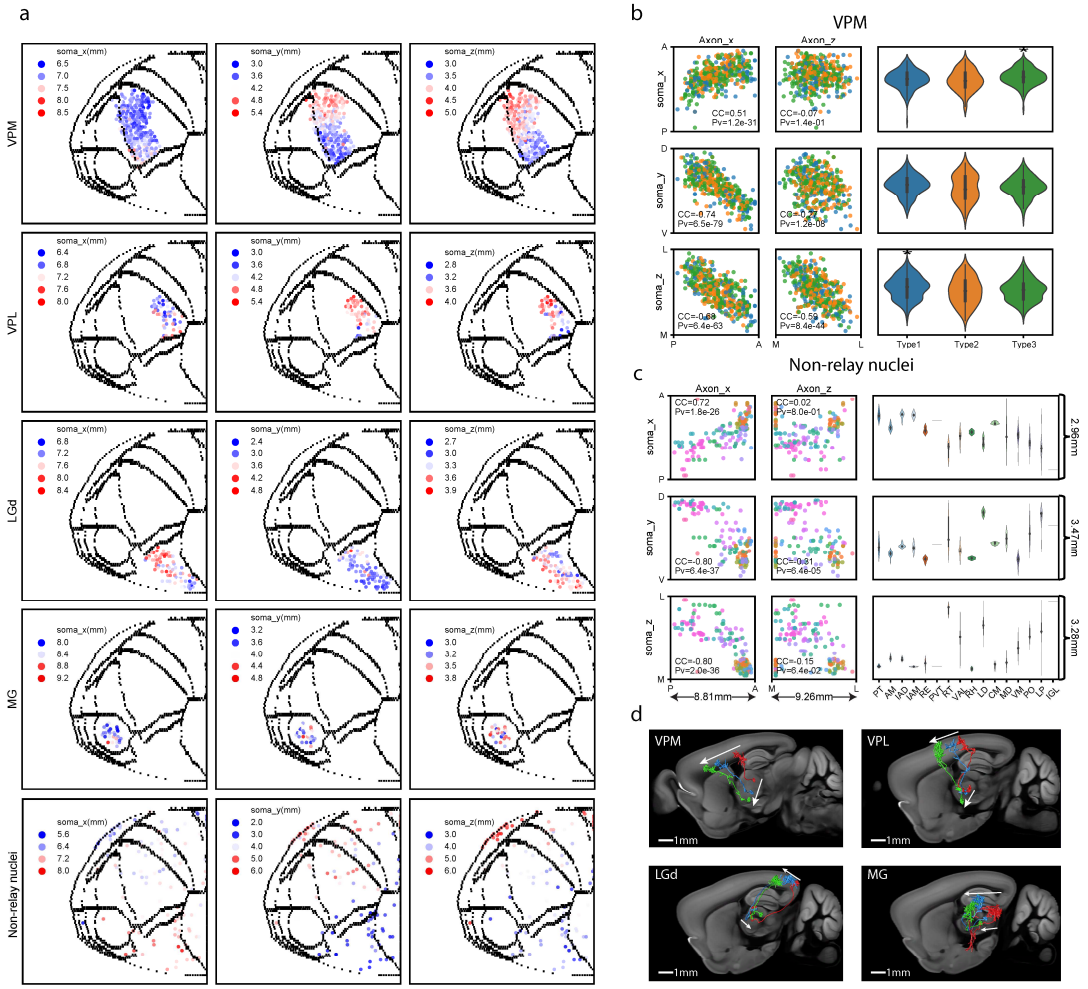

Fig. 5| Topography of thalamic neuron projections by integrating CCF-registered brains.

(a) Location of axon arbors of cortical projecting neurons grouped by thalamic nuclei. Dots represent center of axon arbors in the flattened 2D cortical map. Locations of corresponding soma are color-coded in three separate columns: (left to right) the anterior-posterior (soma-x), dorsal-ventral (soma-y) and lateral-medial (soma-z) axes. (b) (Left panels) Scatter plots showing correlation between soma and axon arbor locations of VPM neurons. Soma axes are defined in the same way as (a). Axon-x and axon-z represent anterior-posterior and lateral-ventral axes, separately. Right panel shows soma distribution of three types of VPM axon arbors. (c) The same layout as (b) but for neurons of non-relay thalamic nuclei. (d) Examples of single neuron projections. Colors represent individual neurons.

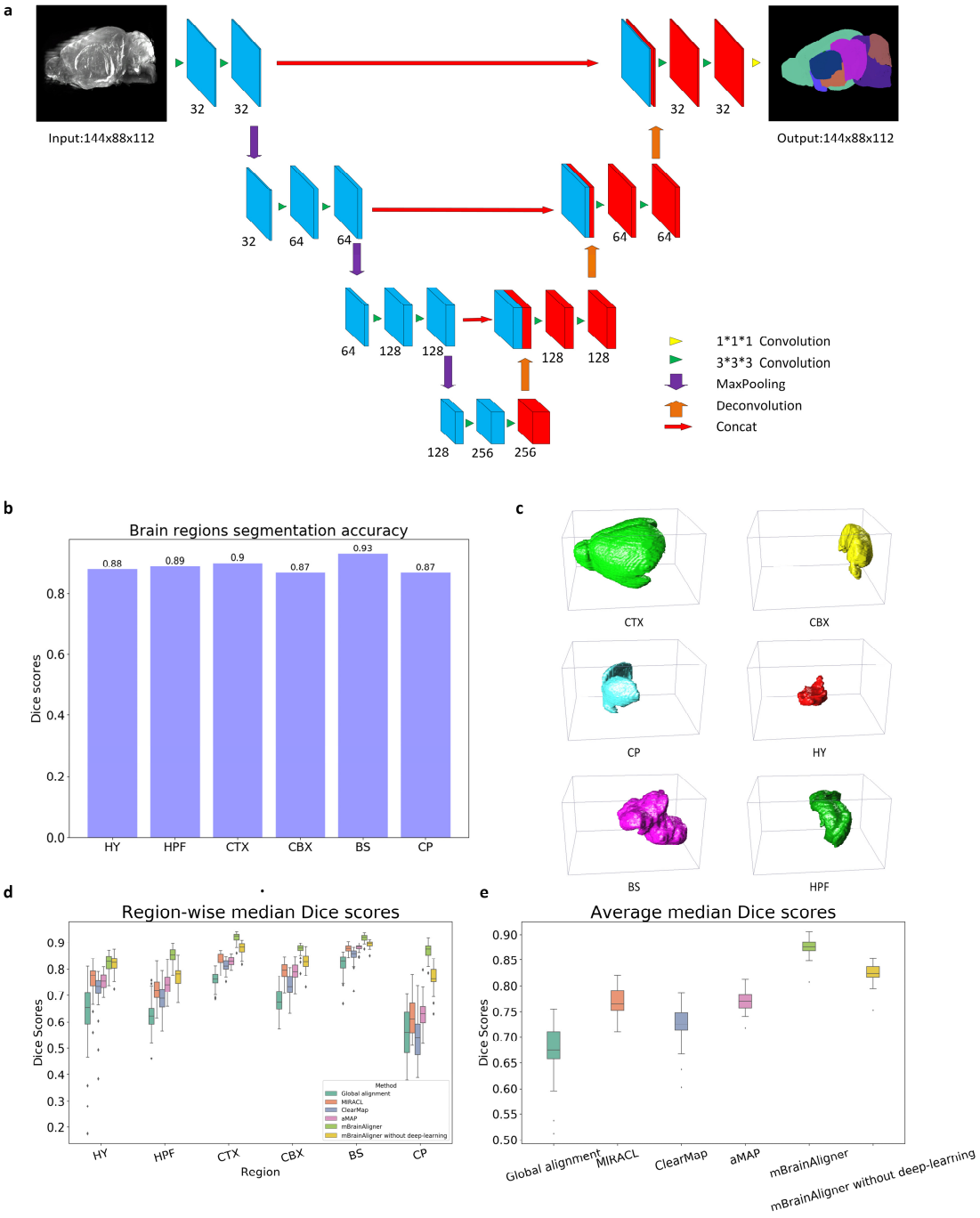

Supplementary Fig. 1| Architecture and performance of deep learning-based segmentation network

(a) Architecture of segmentation network. (b) Segmentation accuracy of six brain regions in terms of Dice scores. (c) 3D visualization of segmentation results of six brain regions. (d)-(e) Comparison of registration accuracy of mBrainAligner with deep learning features toggled on and off. Box plot: center line, median; box limits, upper and lower quartiles; whiskers, 1.5 x interquartile range; points, outliers;

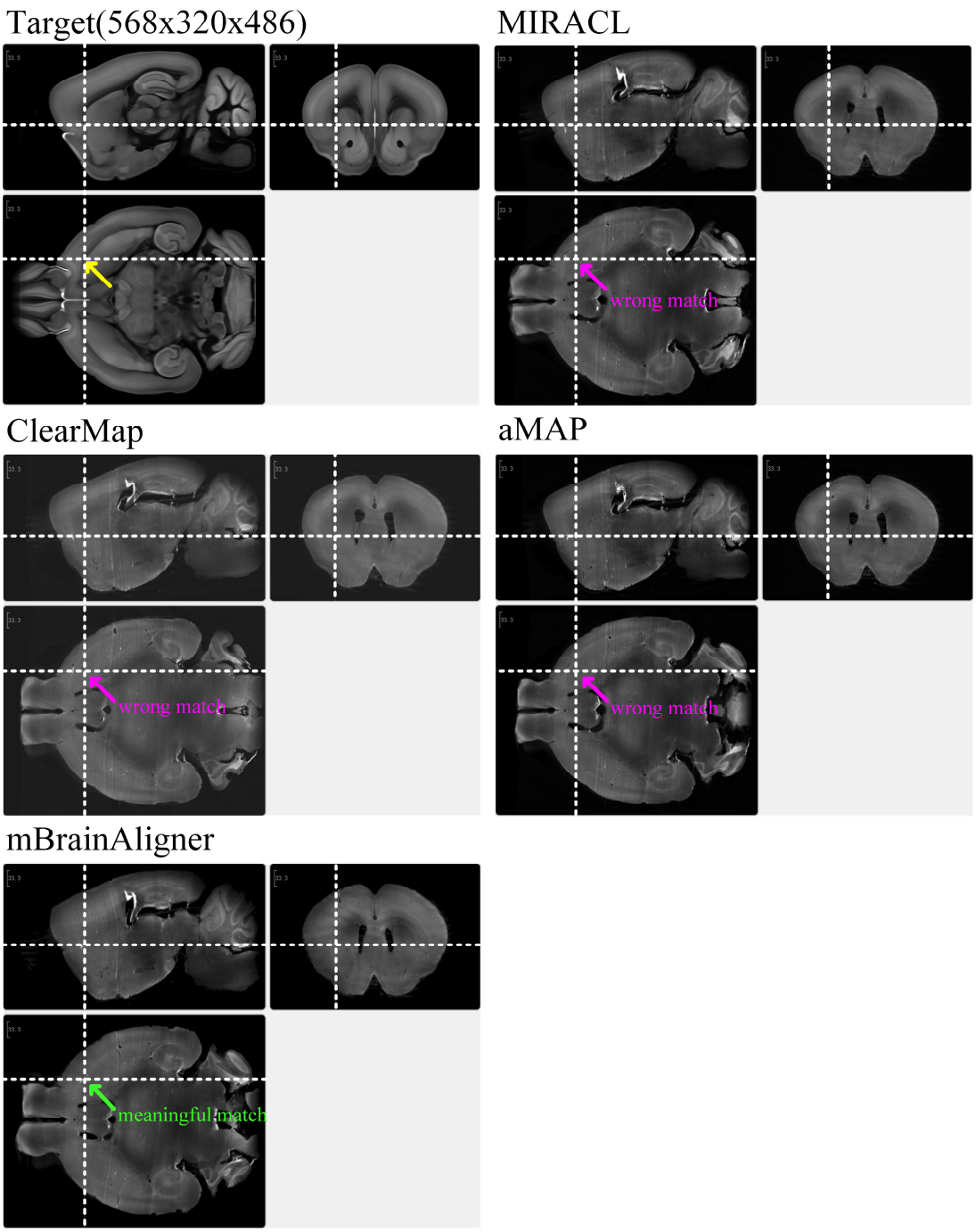
Target(568x320x486)
MIRACL
wrong match
ClearMap
wrong match
aMAP
wrong match
mBrainAligner
meaningful match

(a)

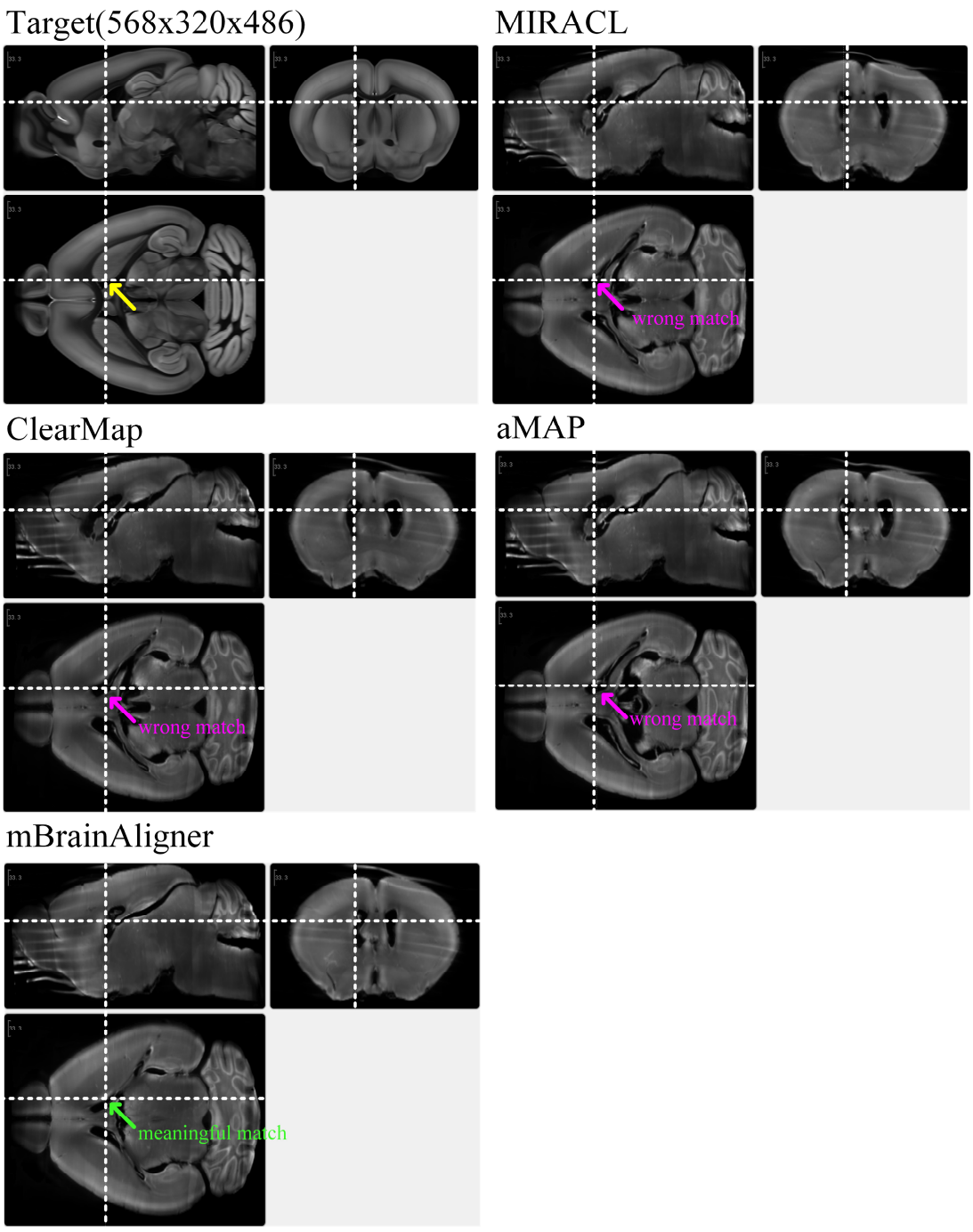

(b)

Supplementary Fig. 2| Comparison of registration results generated by different methods.

(a) and (b) show the registration results of two fMOST brains generated by different methods (mBrainAligner, MIRACL, ClearMap and aMAP). The intersection of dashed lines overlaid on the three-view of aligned brains point to the same space coordinate, with green arrows indicate the meaningful alignment and purple ones for the mismatched results.

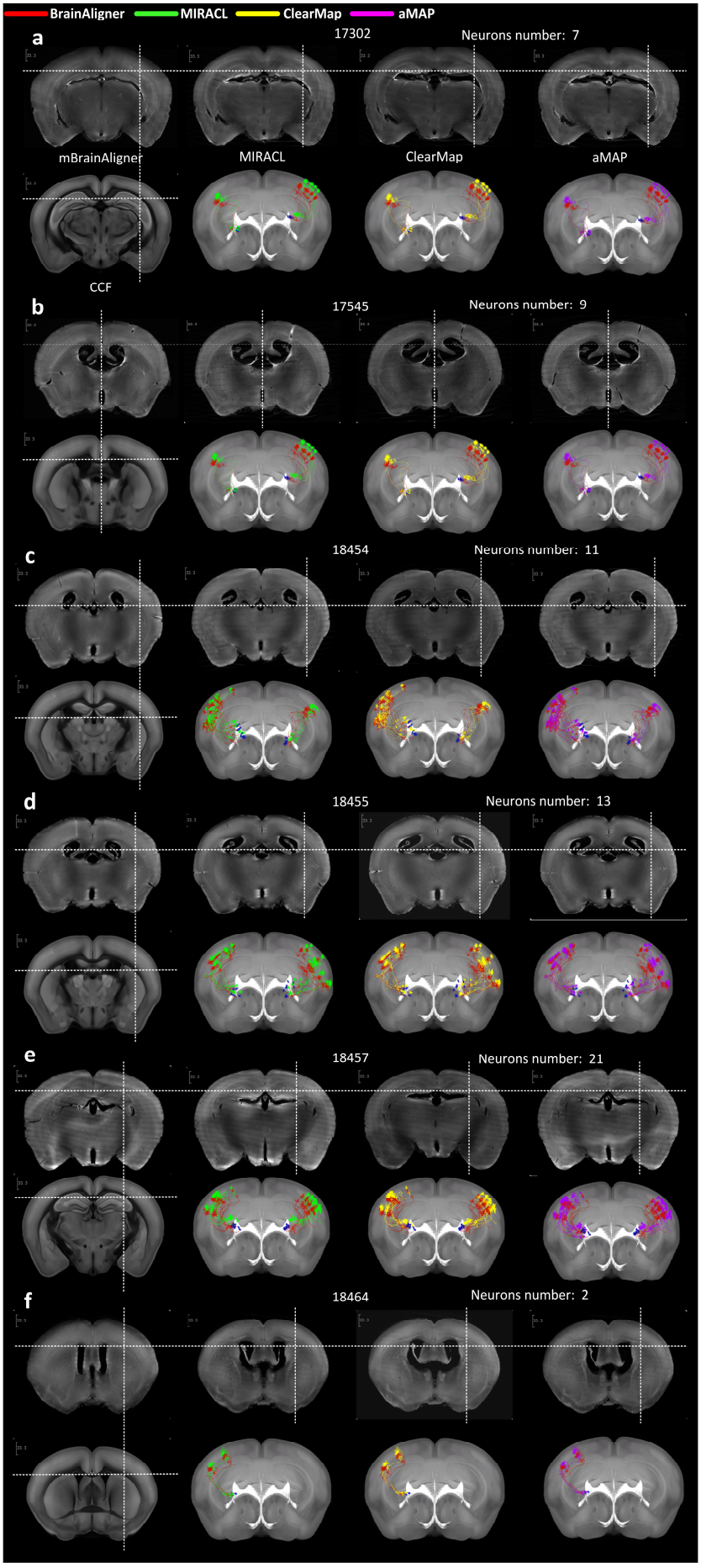
BrainAligner
MIRACL
ClearMap
aMAP
a
17302
Neurons number: 7
mBrainAligner
MIRACL
ClearMap
aMAP
CCF
b
17545
Neurons number: 9
c
18454
Neurons number: 11
d
18455
Neurons number: 13
e
18457
Neurons number: 21
f
18464
Neurons number: 2

Supplementary Fig. 3| Comparison of neuron mapping results generated by different methods.

(a) ~ (f) show 63 CCFv3 mapped neurons of six brains (ID 17302, 17545, 18454, 18455, 18457 and 18464) with somas reside in VPM or VPL. The first row of (a)~(f) show CCFv3 aligned brains generated by four different methods (mBrainAligner, MIRACL, ClearMap and aMAP). The cross-lines overlaid on the aligned brains point to the same coordinate on the inner boundary of cortex. The left-most image of second row of (a)~(f) shows corresponding slice of CCFv3 average template, and the right three images show the maximum intensity projection view of CCFv3 with mapped neurons overlaid, with red for mBrainAligner, green for MIRACL, yellow for ClearMap and purple for aMAP.

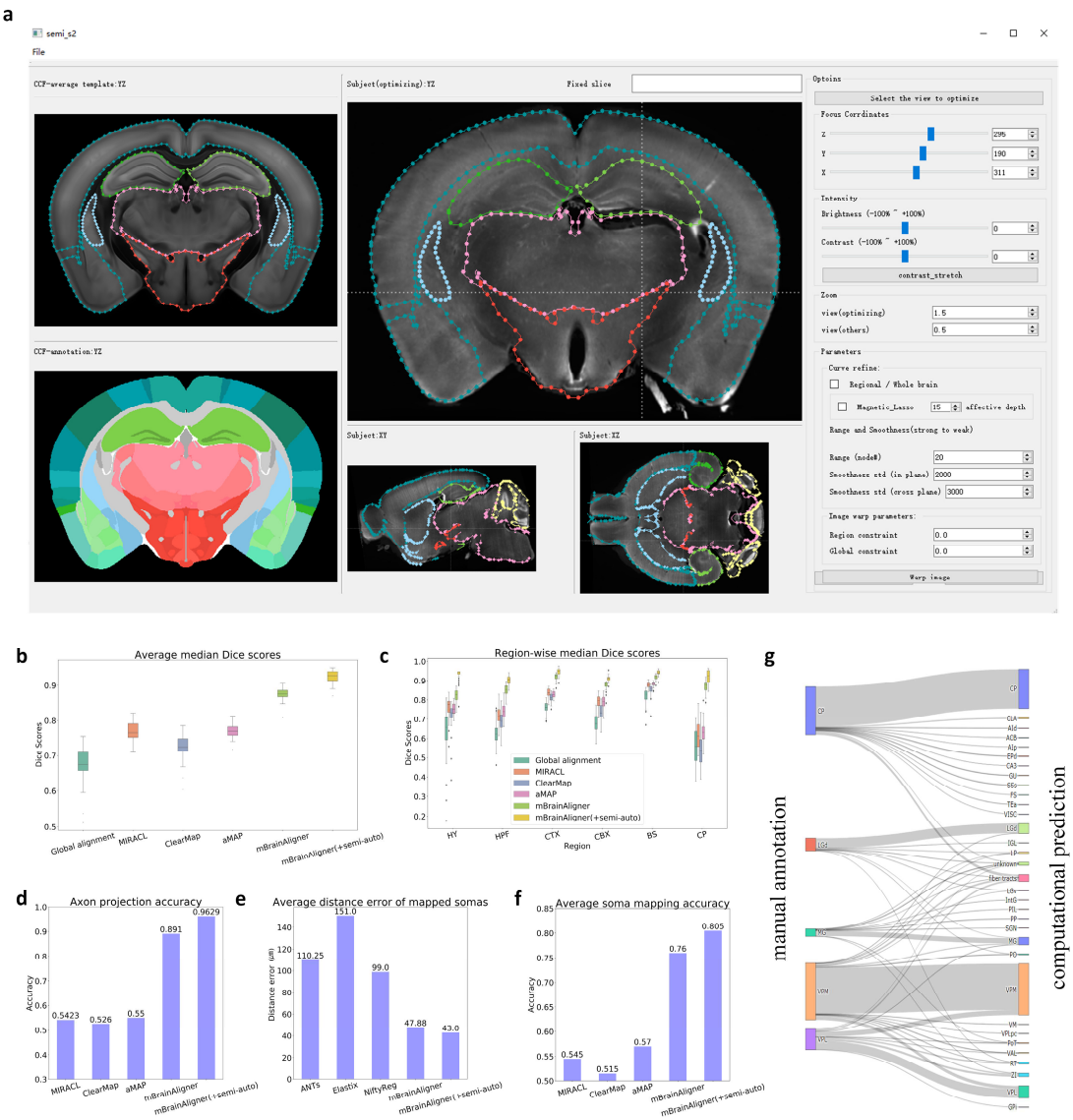

Supplementary Fig. 4| Semi-automatic registration.

Interface of semi-automatic registration module. (b)~(g) Comparison of registration accuracy in different metrics when semi-automatic registration is applied after automatic registration. Box plot: center line, median; box limits, upper and lower quartiles; whiskers, 1.5 x interquartile range; points, outliers;

(a)

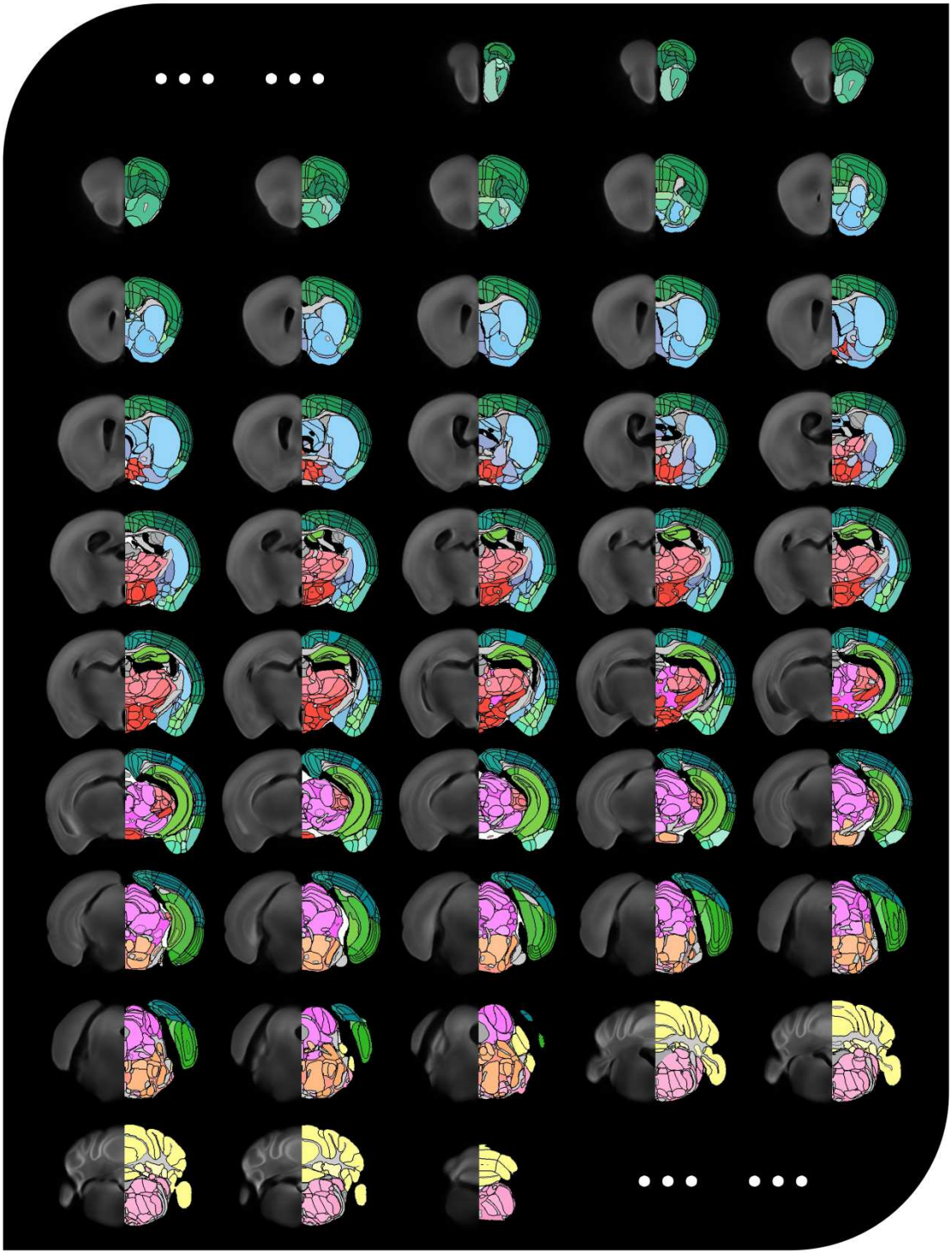

Supplementary Fig. 5| fMOST-domain atlas of mouse brain (2D views)

Coronal sections of fMOST-domain atlas of mouse brain, with average template shown on left and annotation template on right.

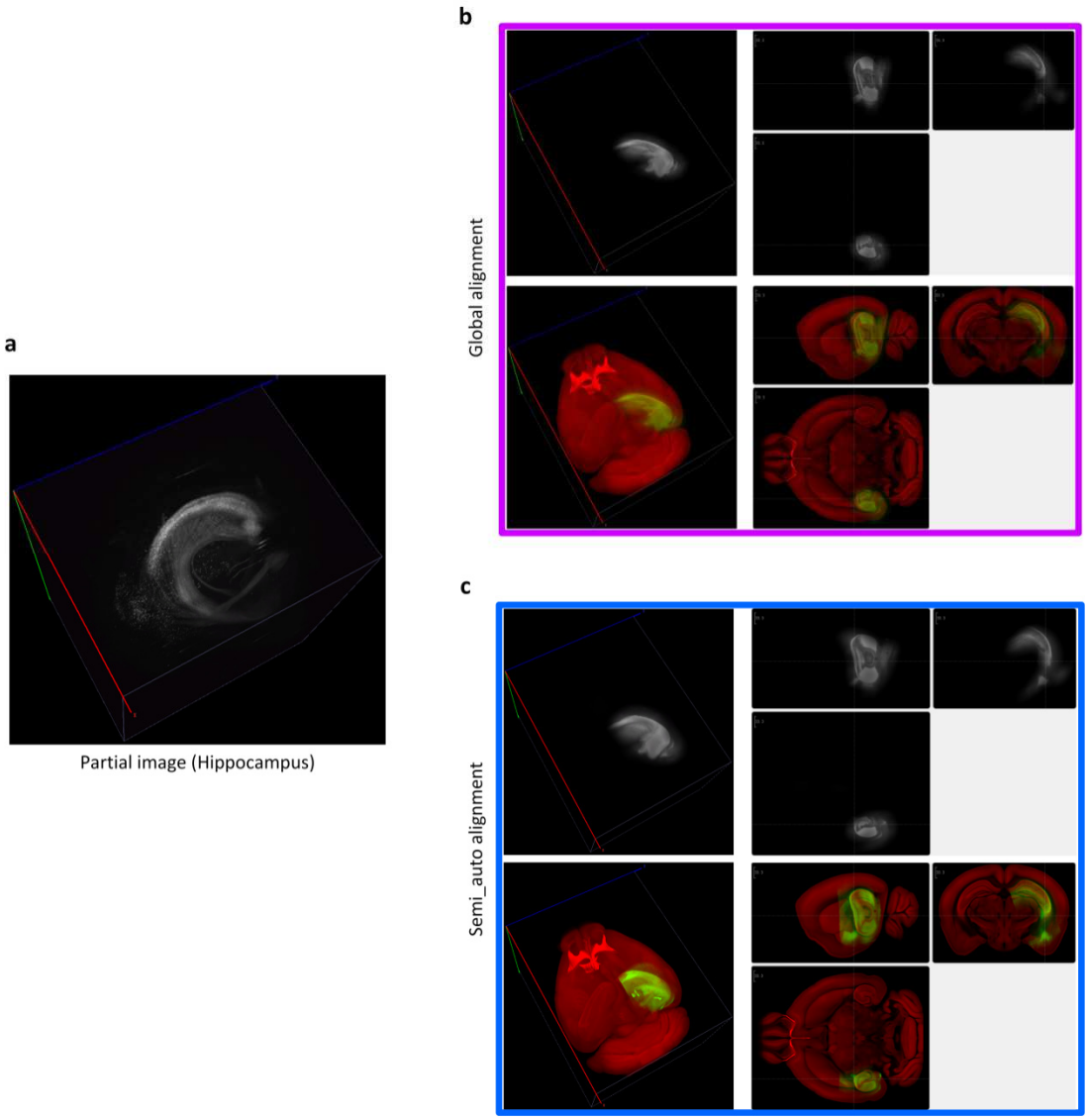

Supplementary Fig. 6| Partial image alignment.

(a) Partially imaged brain region of hippocampus (in LSFM modality). (b) Global alignment result of partial image to CCFv3. The left column show the maximum intensity projection of globally aligned partial brain (top) and its blended view with CCFv3 average template (bottom), with their three-view shown on the right. (c) Result after semi-automatic refinement.

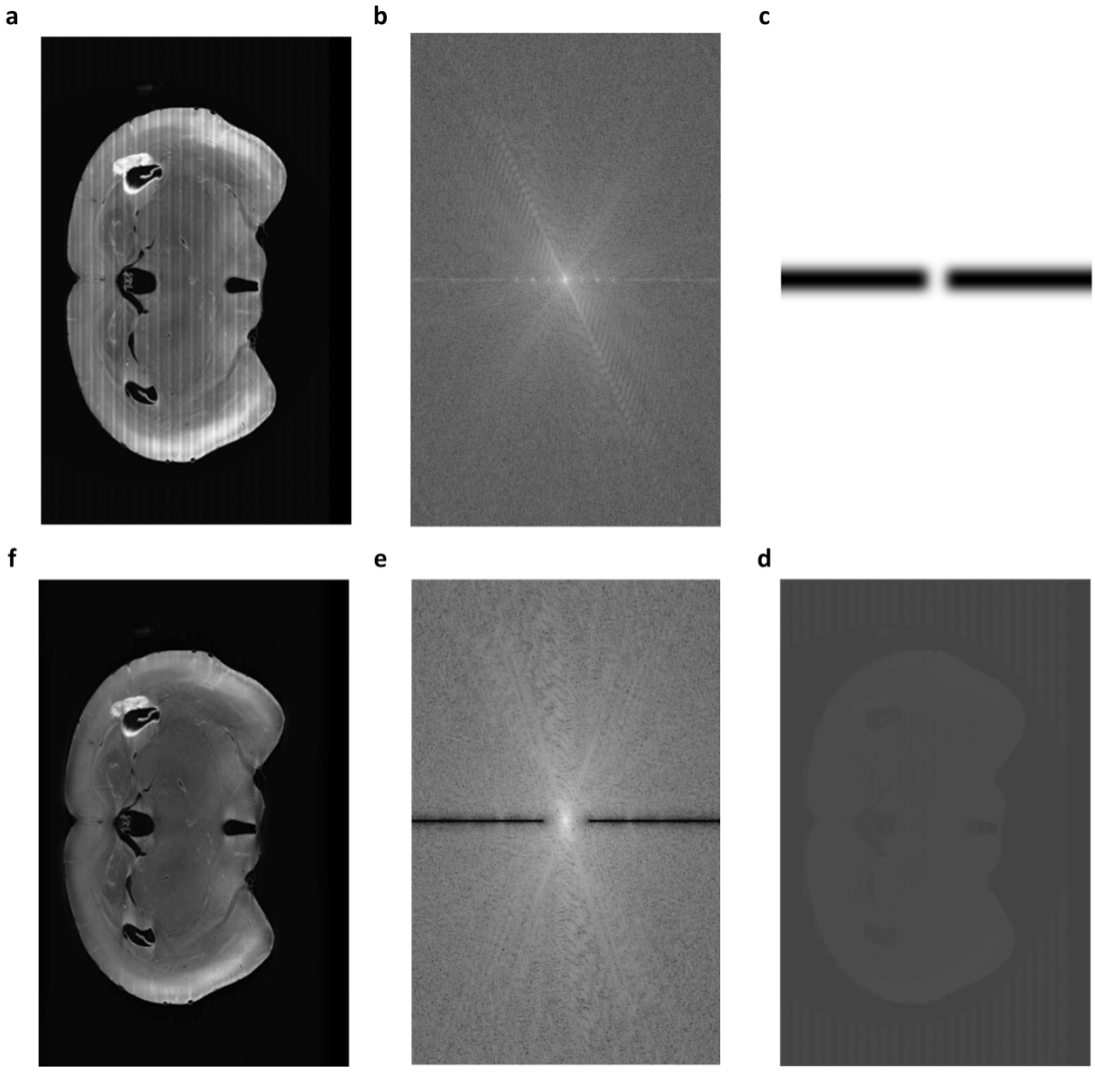

Supplementary Fig. 7| Stripe artifacts removal.

(a) One coronal slice of fMOST mouse brain image. (b) The Fourier spectrum of image shown in (a). (c) Constructed Gaussian notch filter. (d) Log transformed image of (a). (e) Filtered spectrum of log transformed image using filter as shown in (c). (f) Image after stripe removal.

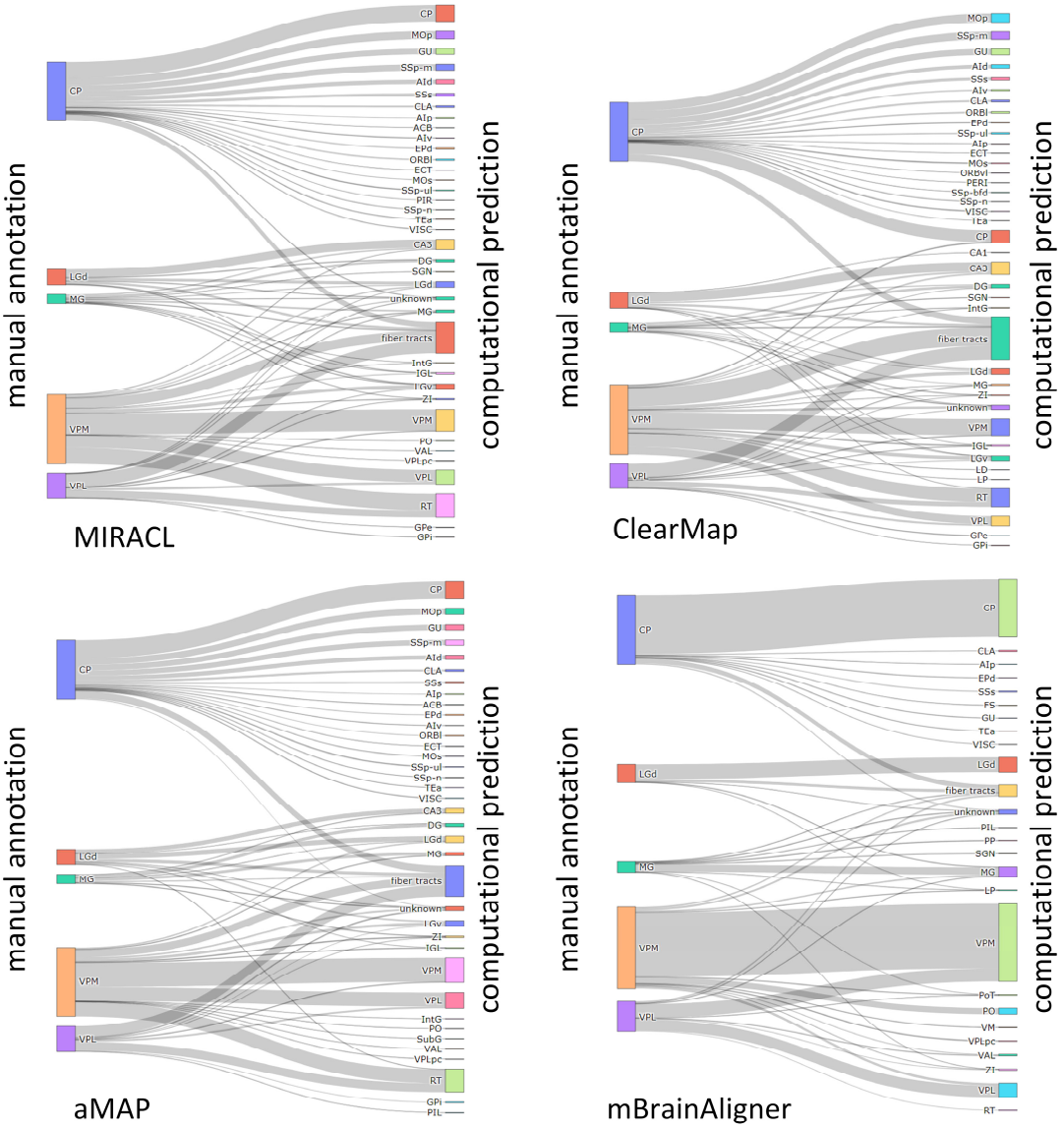

Supplementary Fig. 8| Comparison of soma localization between manual annotation and computational prediction results generated by different methods.

Figures

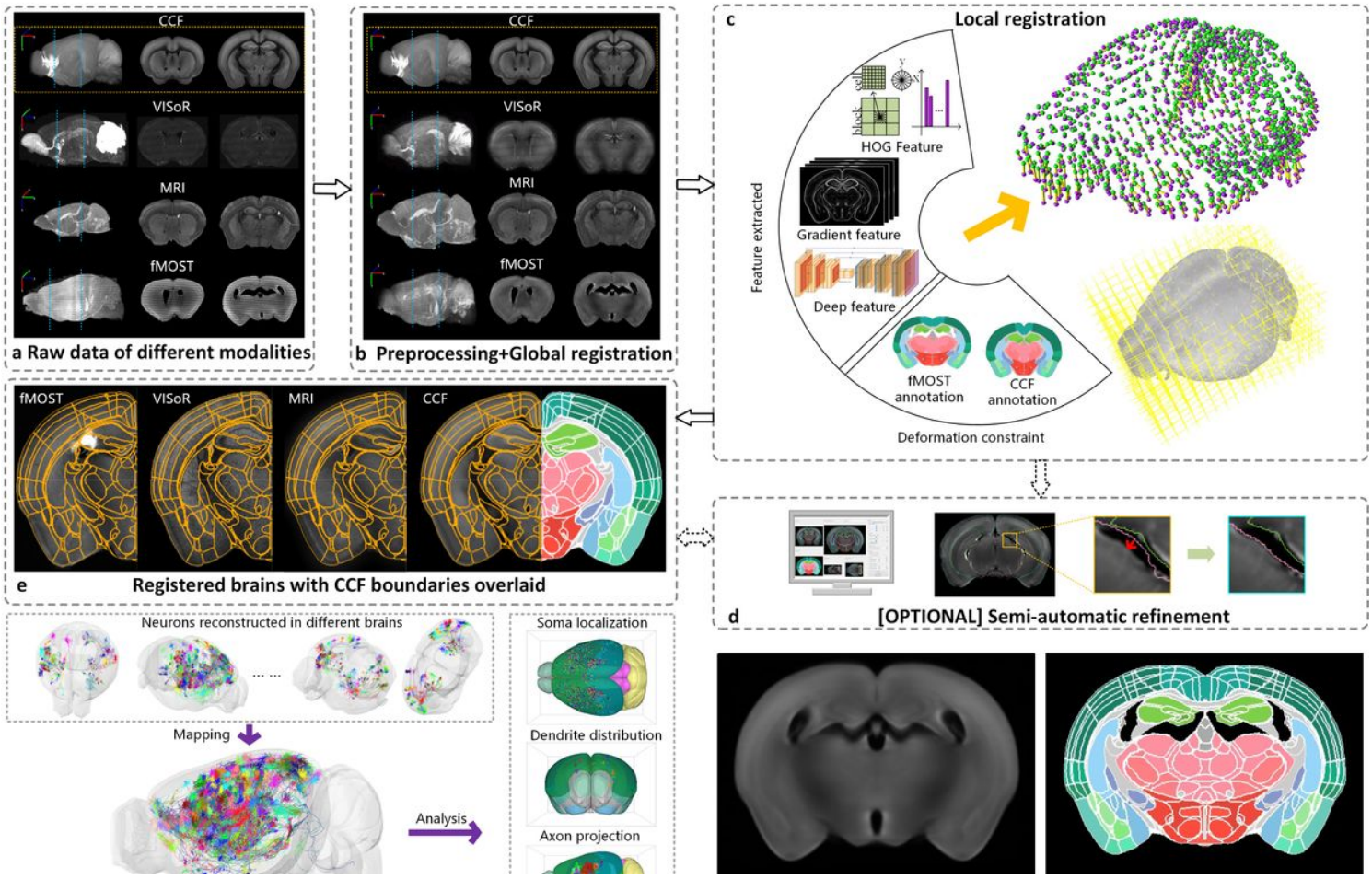

Figure 1

Overview of mBrainAligner for cross-modality image registration, brain delineation, whole brain full morphology neuron mapping, and fMOST mouse brain atlas building. (a) Mouse brain of different modalities exhibit substantial fluctuation in their voxel intensity, image texture, and brain anatomy. The left column shows the maximum intensity projection (MIP) of original brain images of different modalities, two of their coronal slices are shown on the right. (b) Preprocessed and globally aligned brains. For fMOST images, the stripe artifacts were removed before applying global registration. (c) Coherent Landmark Mapping (CLM) based local registration establishes a dense point-by-point correspondence between two images by deforming the target landmarks to fit the subject brains. The landmark deforming is driven by three complementary features (gradient, HOG and deep-learning-derived features) which encode the texture, shape context and semantic information respectively, and constrained by shape priors embedded in atlases. (d) As an optional step, the registration results can be examined and fine-tuned in semi-automatic registration module. (e) Registered brains of different modalities with brain region boundaries defined in CCFv3 overlaid. (f) mBrainAligner enables the mapping of dendritic, axonal, and soma distributions into to a canonical coordinate space for

visualization, comparison and analysis. (g) fMOST domain atlas of mouse brain built with mBrainAligner.

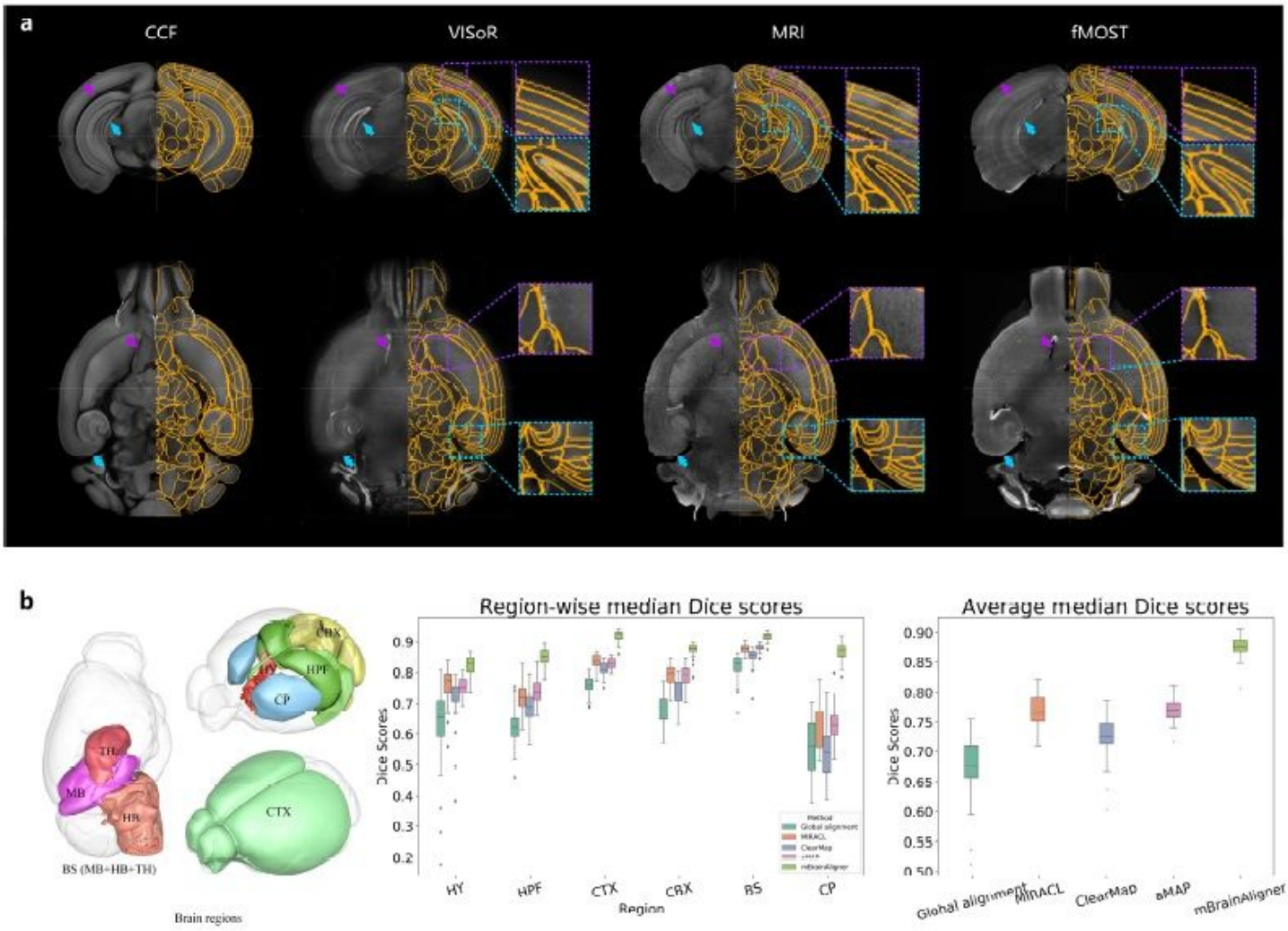

Figure 2

Accuracy of mBrainAligner in brain delineation. (a) Registered brains of different modalities with brain region boundaries (orange) defined in CCFv3 overlaid. The first and second rows show the coronal and sagittal view of registered brains respectively with zoom in view of two subregions. The purple and cyan arrows in the first and second rows point to the same spatial coordinates respectively. (b) Quantitative evaluation of registration accuracy of different methods in terms of region wise and average median Dice scores. The left subpanel shows six brain regions of interest that were annotated by neuroanatomists and used for quantifying the registration accuracy. The middle subpanel shows the region wise median Dice scores and the right subpanel shows the average median Dice scores of different methods. Box plot: center line, median; box limits, upper and lower quartiles; whiskers, 1.5 x interquartile range; points, outliers;

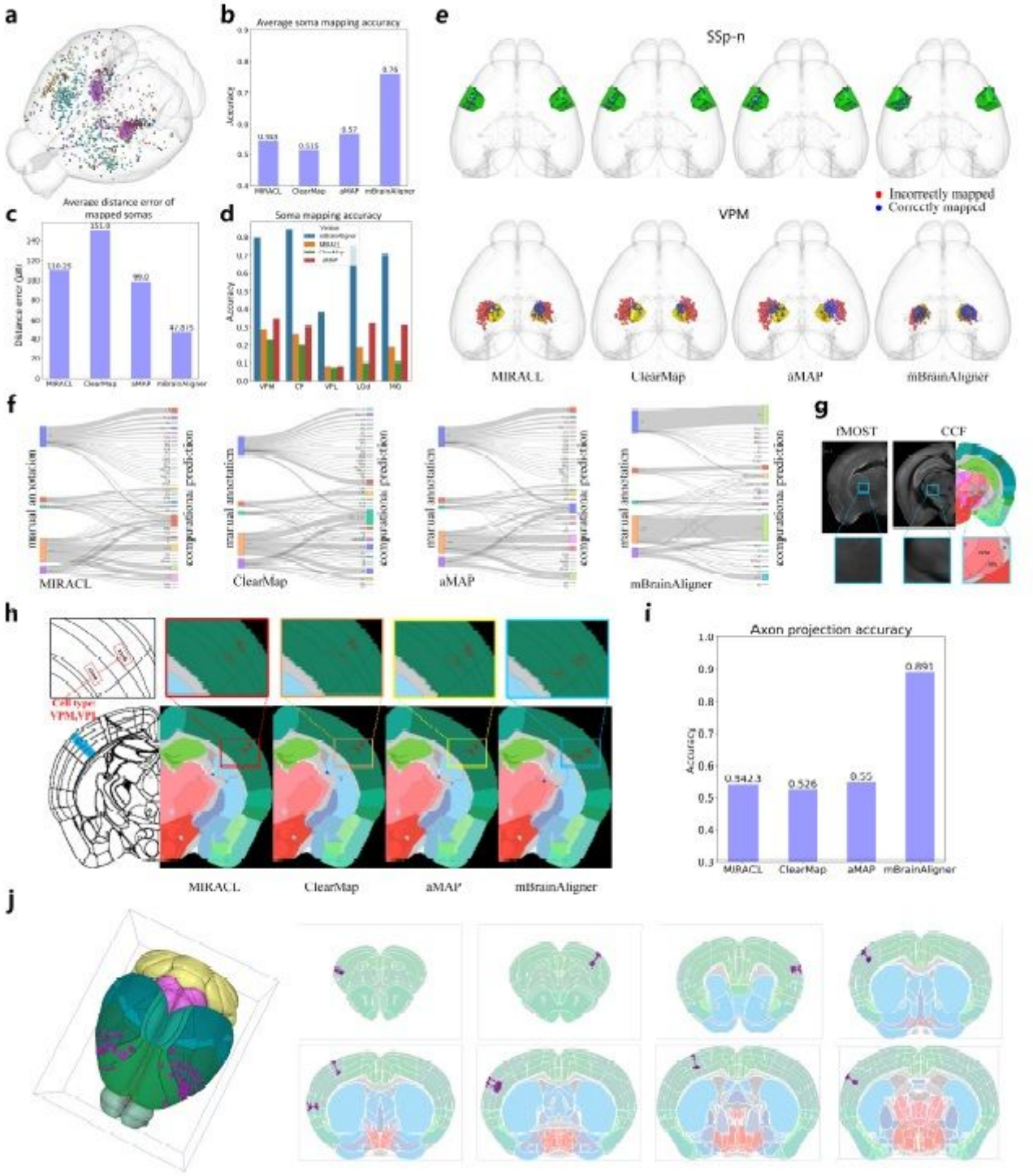

Figure 3

Accuracy of mBrainAligner in computational soma anatomical localizing and axon projection prediction. (a) Distribution of 1708 somas reconstructed from 31 fMOST brains. Different colors represent different brain regions they were manually annotated. (b) Soma mapping accuracy of different methods (MIRACL, ClearMap, aMAP and mBrainAligner). (c) Average distance error of mapped somas of different methods. (d) Comparison of soma mapping accuracy of different methods in five brain regions (VPM, CP, VPL, LGd and MG). (e) Visualization of mapped somas in two brain regions (SSp□n, VPM). The

somas that were mapped outside of their manually annotated region are shown as red dots. Blue dots indicate the correctly mapped ones. (f) Distribution of computational soma localizing results generated by different methods. The left side of diagram shows manually annotated results, and right side shows their computationally predicted results. (g) Zoom-in view of two adjacent small regions (VPM and VPL) where most localization errors occurred. (h) Visualization of axon mapping results of different methods. (i) Computational prediction accuracy of axon projection of different methods on 63 neurons with somas in VPM and VPL. (j) Registered results of 162 neurons with apical dendrites distributed in the L1 layer of cortex. The left-most subpanel visualizes the distribution of neurons in cortex, and other subpanels show the coronal slices with registered apical dendrites overlaid.

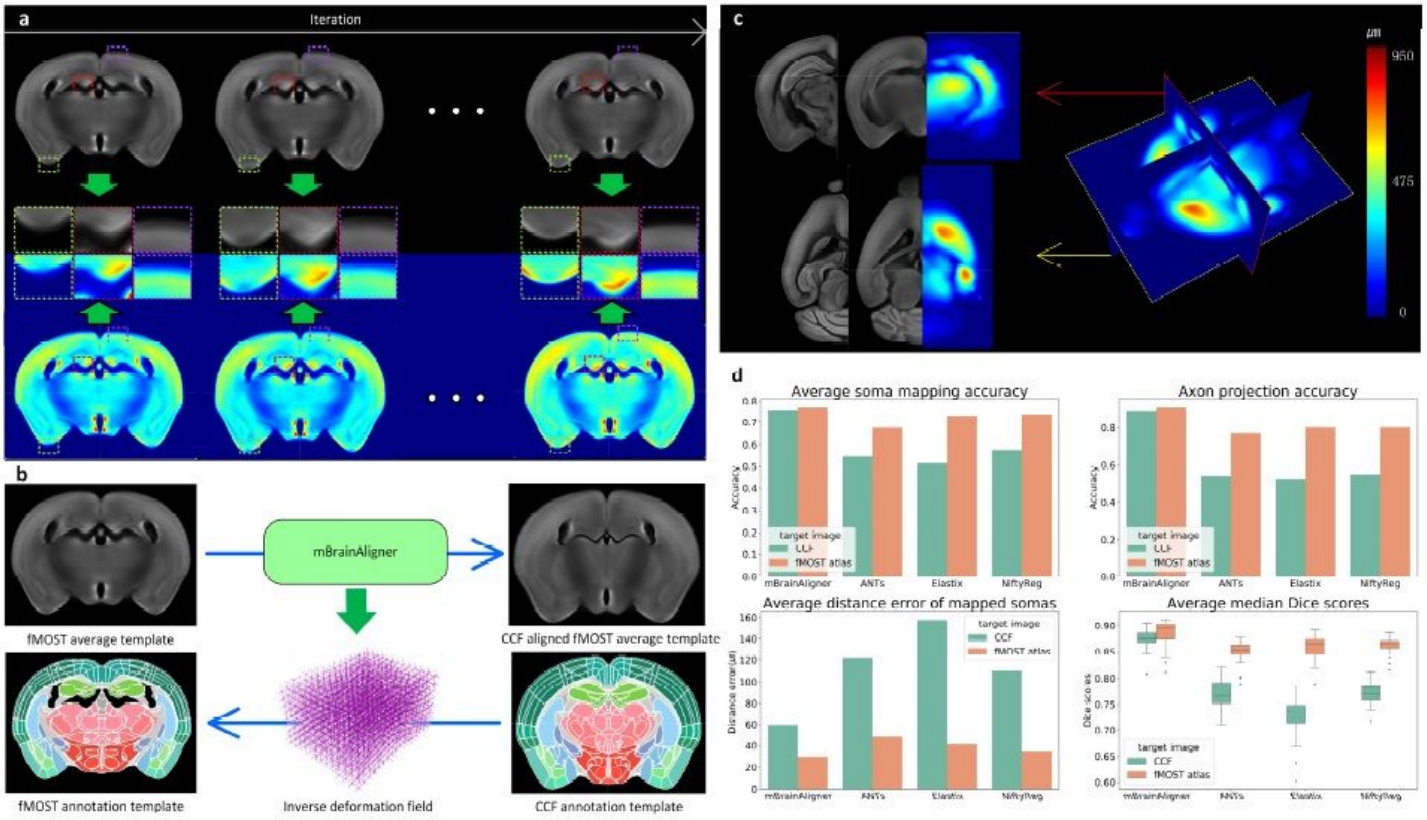

Figure 4

fMOST-domain atlas of mouse brain. (a) Evolution of fMOST average template in the building process. Left to right show results (coronal plane) generated in the 1st, 2rd, and 7th iteration respectively. The top row and bottom row show the gray-scale and color-code visualized atlas, and the close-up views in middle show the sharpness of average template during iteration. (b) Generation of fMOST annotation template. The fMOST average template was first registered to CCFv3 via mBrainAligner. Then, the fMOST annotation template was generated by backward projecting the annotation of CCFv3 using the same warping parameters for image registration. (c) Visualization of anatomical variation between fMOST and CCFv3 atlas. (d) Re-evaluation of registration accuracy of different methods by registering fMOST data to the fMOST atlas. Box plot: center line, median; box limits, upper and lower quartiles; whiskers, 1.5 x interquartile range; points, outliers;

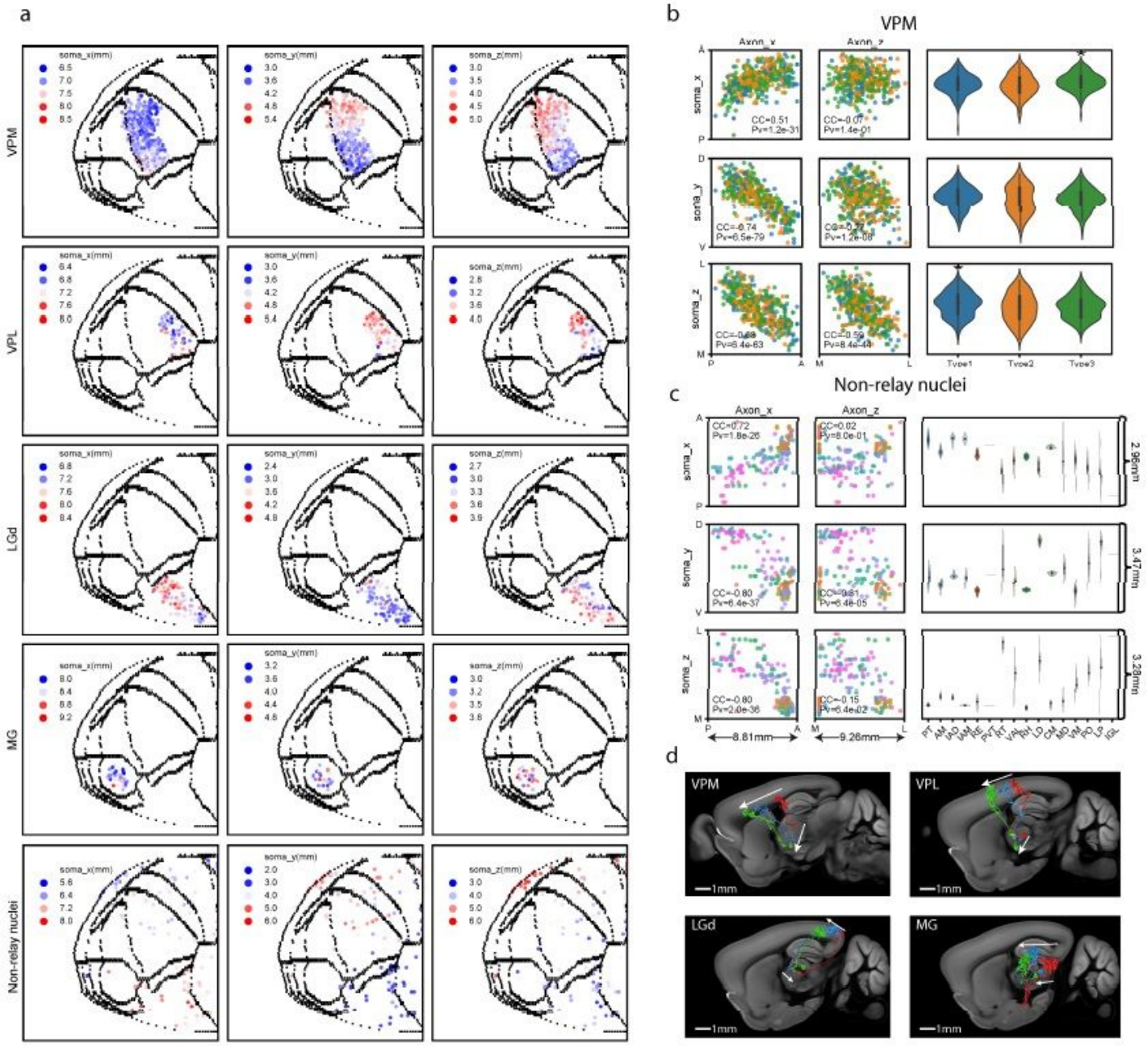

Figure 5

Topography of thalamic neuron projections by integrating CCF‐registered brains. (a) Location of axon arbors of cortical projecting neurons grouped by thalamic nuclei. Dots represent center of axon arbors in the flattened 2D cortical map. Locations of corresponding soma are color‐coded in three separate columns: (left to right) the anterior‐posterior (soma x), dorsal‐ventral (soma‐y) and lateral‐medial (soma‐z) axes. (b) (Left panels) Scatter plots showing correlation between soma and axon arbor locations of VPM neurons. Soma axes are defined in the same way as (a). Axon‐x and axon‐z represent anterior‐posterior and lateral ventral axes, separately. Right panel shows soma distribution of three types of VPM axon arbors. (c) The same layout as (b) but for neurons of non‐relay thalamic nuclei. (d) Examples of single neuron projections. Colors represent individual neurons.

Supplementary Files

This is a list of supplementary files associated with this preprint. Click to download.

- SMovie1.mp4
- SMovie2.mp4
- SMovie3.mp4
- SMovie4.mp4
- flatnreditorialpolicychecklistNMETHA45405A.pdf
- flatnrsoftwarepolicyNMETHA45405A.pdf
- flatnrreportingsummaryNMETHA45405A.pdf